2018

Numerical Study of Interfacial Flow using Algebraic Coupled Level Set-Volume of Fluid (A-CLSVOF) Method

Majid Haghshenas
University of Central Florida

NUMERICAL STUDY OF INTERFACIAL FLOW USING ALGEBRAIC COUPLED LEVEL SET-VOLUME OF FLUID (A-CLSVOF) METHOD

by

MAJID HAGHSHENAS
B.S. Qazvin Islamic Azad University, 2009
M.S. Sharif University of Technology, 2012

A dissertation submitted in partial fulfillment of the requirements
for the degree of Doctor of Philosophy
in the Department of Mechanical and Aerospace Engineering
in the College of Engineering and Computer Science
at the University of Central Florida
Orlando, Florida

Summer Term
2018

Major Professor:
Ranganathan Kumar

ABSTRACT

Solving interfacial flows numerically has been a challenge due to the lack of sharpness and the presence of spurious currents at the interface. Two methods, Algebraic Coupled Level Set-Volume of Fluid (A-CLSVOF) method and Ghost Fluid Method (GFM) have been developed in the finite volume framework and employed in several interfacial flows such as Rayleigh-Taylor instability, rising bubble, impinging droplet and cross-flow oil plume. In the static droplet simulation, A-CLSVOF substantially reduces the spurious currents. The capillary wave relaxation shows that this method delivers results comparable to those of more rigorous methods such as Front Tracking methods for fine grids. The results for the other interfacial flows also compared well with the experimental results. Next, interfacial forces are implemented by enlisting the finite volume discretization of Ghost Fluid Method. To assess the A-CLSVOF/GFM performance, four cases are studied. In the case of the static droplet in suspension, the combined A-CLSVOF/GFM produces a sharp and accurate pressure jump compared to the traditional CSF (continuum surface force) implementation. For the linear two-layer shear flow, GFM sharp treatment of the viscosity captured the velocity gradient across the interface. For a gaseous bubble rising in a viscous fluid, GFM outperforms CSF by almost 10%. Also, a Decoupled Pressure A-CLSVOF/GFM method (DPM) has been developed which separates pressure into two pressure components, one accounting for interfacial forces such as surface tension and another representing the rest of flow pressure. It

is proven that the DPM implementation results in more efficiency in PISO (Pressure Implicit with Splitting of Operators) loop. A two-phase solver is used to study buoyant oil discharge in quiescent and cross-flow ambient. Different modes of breakup including dripping, jetting (axisymmetric and asymmetric) and atomization for cross-flow oil jet are captured.

This thesis is dedicated to my parents Zahra Rouhani and Shirouyeh Haghshenas.

ACKNOWLEDGMENTS

I first wish to acknowledge my advisor, Dr. Kumar for placing complete trust in my abilities, holding my work to such high standard, and providing endless lessons in thinking and working independently.

I also wish to acknowledge my friends and colleagues, James Wilson and Kalpana Madhushan. I would always remember them for thoughtful and motivating conversations while facing new challenges in our research.

Finally, I wish to acknowledge my family. I thank my parents and my brothers, for their support and encouragement throughout my life.

TABLE OF CONTENTS

LIST OF FIGURES x

LIST OF TABLES xiv

CHAPTER 1： INTRODUCTION 1

1.1 Numerical methods for interfacial flows 2

1.2 Cross-flow oil jet 3

1.3 Motivation 4

CHAPTER 2： LITERATURE REVIEW 6

2.1 Two-phase interfacial flows simulation methods 6

2.1.1 Volume of Fluid (VOF) method 7

2.1.2 Level set method 10

2.1.3 Coupled LS/VOF method 11

2.1.4 Interfacial forces implementation methods 12

2.2 Buoyant oil jet in water cross flow 14

2.2.1 Deep sea oil spill 14

2.2.2 Buoyant oil jets 16

CHAPTER 3： NUMERICAL METHODOLOGY 18

3.1 Volume of fluid (VOF) 18

3.1.1 Governing equations 19

3.1.2 Volume fraction algebraic advection 20

3.1.3 Surface tension force 21

3.1.4 Pressure Implicit with Splitting of Operators 21

3.1.5 VOF algorithm 23

3.2 Algebraic coupled level set/volume of fluid 24

3.2.1 Governing equation 25

3.2.2 Coupling VOF and LS method 26

3.2.3 Curvature calculation 32

3.2.4 surface tension force 36

3.3 Ghost fluid method 39

3.3.1 Governing equation 39

3.3.2 GFM-PISO loop 41

3.3.3 Ghost fluid method discretization 42

3.4 Decoupled pressure CLSVOF/GFM 48

3.4.1 Decoupled pressure PISO loop 48

3.5 Turbulence modeling 51

CHAPTER 4： RESULTS 52

4.1 A-CLSVOF method 53

4.1.1 Equilibrium droplet 54

4.1.2 Capillary wave relaxation 58

4.1.3 Rayleigh-Taylor instability and level set advection 60

4.1.4 Droplet impact 65

4.2 A-CLSVOF/Ghost fluid method 69

4.2.1 Static droplet 70

4.2.2 Capillary wave relaxation 72

4.2.3 Linear two-layer shear flow 73

4.2.4 Deformed rising bubble 74

4.3 Decoupled pressure A-CLSVOF/GFM method 76

4.3.1 Static droplet 76

4.3.2 Capillary wave relaxation 78

4.4 Oil jet simulation 79

4.4.1 Oil jet in quiescent water 80

4.4.2 Oil jet in cross-flow 86

CHAPTER 5： CONCLUSION 96

LIST OF REFERENCES 100

LIST OF FIGURES

Figure 1.1 Ligament formation in a spray atomization flow [1]. 2

Figure 1.2 Spray jet simulation using level set method [2]. 4

Figure 2.1 Volume fraction α distribution in VOF method. 8

Figure 2.2 Distance function distribution in the LS method. 11

Figure 2.3 Schematic diagram of breakup modes for liquid discharged upward into another liquid medium reported by experimental researchers. 17

Figure 3.1 Flow diagram of VOF method for one computational cycle. 24

Figure 3.2 1D discretization of volume fraction (left) and the distance function calculated by Eq.3.34 (right). 31

Figure 3.3 Comparison of the reinitialization methods (a) this study: A-CLSVOF, and (b) S-CLSVOF 32

Figure 3.4 Flow diagram of A-CLSVOF method for one computational cycle. 38

Figure 3.5 Schematic of 2D computational stencil where the interface locates between C and E, and C and N. 44

Figure 3.6 Flow diagram of A-CLSVOF/GFM method for one computational cycle. . . . 47

Figure 3.7 Flow diagram of decoupled pressure A-CLSVOF/GFM method for one computational cycle. 50

Figure 4.1 (a) Plot of U_{max} as a function of time, (b) comparison of pressure distributions at centerline and, for fine grid of $\Delta x = 1mm$. 57

Figure 4.2 Time evolution of capillary wave amplitude compared with analytical solution for grid 64^2. 59

Figure 4.3 Comparison of Rayleigh-Taylor instability evolution, (solid background) current A-CLSVOF model and (representation with local gridrefinement) Zuzio and Estivalezes. . . 62

Figure 4.4 Time evolution of 3D Rayleigh-Taylor instability simulation. 63

Figure 4.5 Number of reinitialization solution and LS field error versus time. 64

Figure 4.6 Grid independence study on interface height variation. b) Comparison of our numerical interface time evolution with experiments. 67

Figure 4.7 Qualitative comparison of our numerical result and experimental result of interface evolution. 69

Figure 4.8 Pressure distribution of a static 2D drop after 10 time steps. Density ratio is $\rho_l/\rho_g = 10$, a) GFM and b) CSF. 71

Figure 4.9 Capillary wave oscillation versus time. The GFM result is compared with the analytical solution. 73

Figure 4.10 Steady state horizontal velocity profile predicted by CSF and GFM treatment of viscous term. 74

Figure 4.11 Temporal evolution of the droplet velocity U_d for different singular term implementation. The present simulation result is compared with experimental terminal velocity. . 75

Figure 4.12 Comparison of pressure distributions at centerline for different methods. 78

Figure 4.13 Comparison of DPM and segregated GFM in number of iteration for the case of capillary wave relaxation. N_c represents number of correction in PISO loop. 79

Figure 4.14 Comparison of present study simulation (bottom row) with respect to the result of Homma et al. (top row, left sides) and experiment Song et al. (top row, right sides). 81

Figure 4.15 Comparison of capillary jet simulation (axisymmetric jetting breakup mode) of this study (left) with reported experimental result (right). 83

Figure 4.16 Qualitative validation of our jetting mode simulation (second and fourth from left) compared to empreimental (fisrt and third from left) results by Peng et al. 84

Figure 4.17 High Reynolds straight oil jet (atomization) simulation result for different injection velocities. 86

Figure 4.18 Schematic view of the considered domain for cross flow simulation. 87

Figure 4.19 Different modes of breakup for an oil jet in cross-flow water for $J = 3.5$ a) dripping $Re_j = 70$ b) axisymmetric jetting $Re_j = 350$ c) asymmetric jetting $Re_j = 760$ d) atomization $Re_j = 2200$. 88

Figure 4.20 Time evolution of different modes of breakup for an oil jet in cross-flow water: dripping, axisymmetric jetting, asymmetric jetting and atomization. 89

Figure 4.21 Effect of cross-flow momentum of discharged oil for $Re_j = 968$, $We = 25$: a) $J = 22.4$ b) $J = 9.9$ c) $J = 5$ d) $J = 3.5$. 90

Figure 4.22 Regime map of different modes of breakup for an oil jet in cross-flow water based on mpmentum ratio J and jet Rynolds number Re_j. 91

Figure 4.23 Effect oil viscosity on breakup dynamics by cosidering four real oil types: a) Heptane $Re_j = 4300$, $We_j = 32.5$ b) Kerosene $Re_j = 960$, $We_j = 30.1$ c) Mars TLP $Re_j = 91.8$, $We_j = 44$ d) Platform Gail $Re_j = 15.4$, $We_j = 46.1$. 92

Figure 4.24 Effect oil surface tension on jet breakup pattern by considering Kerosene oil with different surface tension coefficients and accordingly Weber numbers: a) $We_j = 22.25$ b) $We_j = 27.81$ c) $We_j = 37.08$ d) $We_j = 55.62$. For all the cases Reynolds is the same as $Re_j = 968$. 93

Figure 4.25 Regime map of different modes of breakup for a wide range of We_j and $\beta = mu_j/\mu_c$, for different momentum ratios, $J = 2$ and $J = 3.5$. 95

LIST OF TABLES

Table 3.1 Comparison of different curvature values using three different normal calculations for a droplet with a curvature of $40m^{-1}$. 36

Table 3.2 Comparison of error for the indicator field, λ using three methods. 37

Table 4.1 Study of spurious currents and pressure error between three methods. 56

Table 4.2 Relative error E_2 for capillary wave time evolution for different methods. 60

Table 4.3 Parasitic currents and pressure comparison (at 50 time steps) between CSF and GFM. 71

Table 4.4 Parasitic currents and pressure comparison (at 50 time steps) between CSF, GFM and DPM. 77

Table 4.5 Properties of different oil types used in our simulation. 82

Table 4.6 Present study length of breakup L_b compared to result reported by reported experiments. 83

CHAPTER 1
INTRODUCTION

Multiphase flows play an important role in many natural phenomena and industrial applications. Generally, every fluid flow with more than one phase or component is called multiphase flow. There is a wide spectrum of multiphase flows in nature. Multiphase flows in a general classification are classified as interfacial flows and mixtures. For the interfacial flows, the discontinuity is important like a single droplet, while for the mixture flow, the whole flow is treated as one fluid with new averaged properties. Also, according to the state of different phases and components, multiphase flow can be categorized as gas-solid, liquid-solid, liquid-gas, liquid particles and etc. [1, 3].

Scientists have been interested in the different tools to get better understanding on two-phase flows dynamics and predict the behavior for the engineering designs. From the analytical aspect, two-phase flows are notably difficult to model, since the governing equations are nonlinear and the interface position (transition region) needs to be tracked. Therefore, analytical solutions are limited to simple flows [4]. Also, the experimental study is unlikely for many two-phase flows, because of model length scale, short time scale, limited optical access and experimental cost. While the experimental and analytical studies are not always achievable, computational fluid dynamics is the best technique for confident exploration of two-phase phenomena.

Figure 1.1: Ligament formation in a spray atomization flow [1].

1.1 Numerical methods for interfacial flows

Computational Fluid Dynamics (CFD) is an appropriate technique to study a wide spectrum of multiphase flows. In particular, interface tracking and modeling property discontinuity have been the main challenges in two phase flows. Several mathematical and numerical models have been developed to gain better understanding of interfacial flows in various scientific and industrial applications. These models could be categorized into two groups where fixed and moving grids have been used. For the moving grid methods, the interface is treated as a boundary which separates the main domain into sub-domains [5]. For the fixed grids, the whole computational domain is solved as a mixture fluid whose phases are distinguished by a scalar indicator function. The fixed grid methods include the Lagrangian front tracking method proposed by Unverdi and Tryggvason [6] and the Eulerian interface capturing methods such as volume of fluid (VOF) [7], Level Set

[8], phase field [9] and the most recent moment of fluid (MOF) [10]. Each of these well-known methods has its virtues and drawbacks. Coupled methods have some advantages over traditional methods. For instance, coupled level set volume of fluid (CLSVOF) method is mass conservative like VOF and smooth at the interface like LS method [11]. A coupled level set- moment of fluid (CLSMOF) has also been proposed recently to incorporate the benefits of the moment of fluid and the level set for interface reconstruction [12].

1.2 Cross-flow oil jet

Worldwide deep-sea oil/gas exploration takes place at increasingly deeper locations to meet the expanding needs of oil and gas for various applications. There is high potential for well blowout or oil leakage during these operations. In addition, this situation could become more complicated by factors such as hydrate formation, high pressure and cold ambient fluid, and compressible gas dissolution [13]. The oil spill in the deep sea could be simplified as an immiscible jet penetration in a water cross-flow. Generally, the term jet in cross flow refers to a jet of fluid discharging from a nozzle into a cross-flowing surrounding fluid. Many numerical and experimental studies have been performed on the oil jet in cross-flow in order to understand the physical behaviour of this important type of flow.

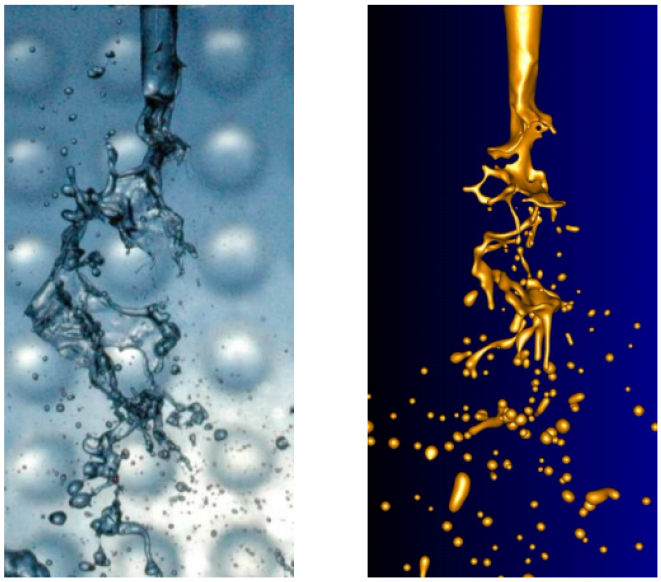

Figure 1.2: Spray jet simulation using level set method [2].

1.3 Motivation

Although many reliable methods have been developed to simulate liquid-liquid and gas-liquid systems, researchers are still looking for new techniques to improve simulation accuracy and stability, and decrease the computational cost. There are advantages and disadvantages with each proposed method, for instance, the Volume of Fluid (VOF) method has reported high spurious velocity at the interface because of volume fraction sharp transition. Decreasing these errors in simulation is a challenge for numerical researchers. Also, the Level Set (LS) method shows considerable mass conservation issues which needs to be treated. Therefore, researchers are interested in coupling methods to improve the state of art two-phase flow CFD techniques.

On the cross-flow oil jet, our understanding of the underlying physics is partial. Experimental and numerical studies could substantially improve our knowledge to complement modelling efforts. The CFD study on the oil spill would provide crucial information on the phenomena which is not feasible using experimental techniques.

CHAPTER 2
LITERATURE REVIEW

In this chapter, an overview of the two-phase flow CFD methods has been carried out to achieve such comprehensive view on previous methods, followed by a survey on previous works on cross-flow oil spill phenomena including numerical and experimental researches. As mentioned in the introduction, two-phase flow simulation began in early sixties, however most promising methods such as VOF, LS and Front Tracking were introduced in the eighties and nineties along with developing computers. The oil spill studies has been mostly focused on high density ratio fuel in air jets, and less on buoyant oil jet in water cross flow.

2.1 Two-phase interfacial flows simulation methods

In this section, we review previous publications on the two-phase flow methods including VOF, LS and CLSVOF which are related to our work. Next, we explore two primary methods, continuum surface force (CSF) and ghost fluid method (GFM), for implementation of interfacial forces including surface tension, buoyancy and viscous.

2.1.1 Volume of Fluid (VOF) method

The VOF method, which is mass conservative, was first introduced by Nicholas and Hirt in 1981 [7] . In this method, the volume fraction field ($\alpha \in 0,1$) is transported to identify the new interface location/contour which exists in partially filled cells where ($0< \alpha <1$). The volume fraction indicates the ratio of the liquid volume to the total cell volume where partially filled cells contain some value of. The volume fraction between 0 and 1 and implies that the immiscible phase interface plane/contour lies somewhere within the cell (Fig. 2.1). Generally, in VOF methods, the advected volume fraction is used to calculate the interface curvature which is proportional to the surface tension force. In finite volume methods, this surface force is converted to a volume force by some delta function quantifying the local interfacial area per unit volume. This quantity is then passed to the momentum equation as a source term where the new pressure and velocity fields are eventually calculated.

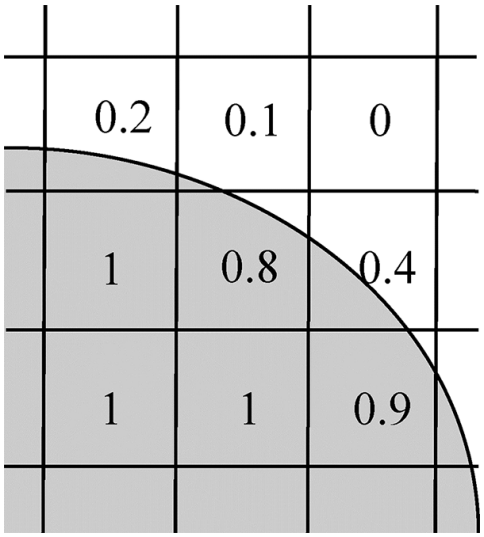

Figure 2.1: Volume fraction α distribution in VOF method.

There are two common approaches to advect the volume fraction; these are commonly referred to as geometrical and arithmetical advection schemes. In the geometrical advection methodology, the interface is reconstructed, using the volume fraction at each cell and its neighboring cells, to approximate the interface plane specification including the normal vector and the intersection lines with the cell faces. Most common interface reconstruction techniques are simple line interface calculation (SLIC) by Noh and Woodward [14], and piecewise linear interface calculation (PLIC) by Youngs [15] and Ashgriz [16]. Rider and Kothe [17] gathered a comprehensive review on PLIC interface reconstruction methods before 1998. Next, more reliable methods such as efficient least square interface reconstruction algorithm (ELVIRA) by Pilliod [18] and parabolic reconstruction of surface tension (PROST) by Renardy and Renardy [19] reported higher order of accuracy to avoid numerical errors, particularly spurious currents. Also, Lopez et al. proposed an advanced

method of spline-based interface reconstruction (SIR) which was limited to 2D [20]. The primary geometrical VOF advection methods used flux-split advection schemes restricted to the principle coordinate axes and caused the formation of flotsam/jetsam and also the onset of parasitic currents. To deal with this problem, Pilliod and Pucket [21] proposed an un-split advection scheme, which was also second order accurate. Then, Lopez et al. [20, 22] introduced an advanced multidimensional un-split advection technique, which was recently extended for 3D by Owkes and Desjardins [23] where the fluxed volume fraction (regions where the flux region overlaps with the geometrically reconstructed liquid volume regions) of local and neighboring regions are used in determining the rate of filling/emptying of the liquid volume in each cell.

VOF method initially used surface marker for surface tension force, however Brackbill et al. [24] used divergence of volume fraction function to calculate curvature at the interface and proposed continuum surface force (CSF) method, which is explained in next section. Later, Lafaurie et al. [25] extended the previous technique to conservative CSF. The VOF method has been developed in many aspects, accurate advection [22] improved surface tension calculation [19, 26] and more accurate momentum equation discretization [27]. In the arithmetic advection methods, a compressive velocity is commonly utilized to reduce excessive diffusion of the volume fraction at the interface [28] resulting from flux splitting and absence of accurate geometric interface location data. The compressive term ensures the sharpness of the interface which helps to diminish the onset of flotsam/jetsam and also spurious currents. The most commonly used and modified arithmetic advection implementation using flux splitting and compressive velocities is implemented in

in the OpenFOAM framework [29, 30]. Deshpande et al. [31] assessed this solvers capabilities for modelling immiscible two-phase flows.

2.1.2 Level set method

Level Set (LS) is a commonly used method, initially introduced by Osher and Sethian [8], while Sussman et al. [32] further developed it for the two-phase flows simulation. In the LS method, a signed distance function is said to exist such that the magnitude of its value at any point in the domain defines the shortest normal distance to an interface and where the interface curve/surface is defined as the zero level set of this field (Fig. 2.2). Generally, this distance function becomes positive in the liquid phase and negative in the gas phase. Traditionally, the distance function is not solved for implicitly, but is determined by minimizing the error in the gradients iteratively (see section describing redistancing). Since the LS field is a signed distance function, its gradient points towards the nearest interface (from the gas phase) and also possesses a magnitude of unity with units of [m/m], making it a primary candidate for defining the interface normal orientation. After the initial calculation of the distance function, it is advected to determine the new interface location and resulting surface tension force but only after the reinitialization procedure is executed since the advected function generally does not remain a signed distance function. Osher and Fedkiw [33] gathered an overview on initial efforts in the Level Set development.

The advection/reinitialization in the LS method cause mass loss in the simulation as the interface location, or the zero level set, drifts from the actual location; this is known to be the main

deficiency of the Level Set method. It should be noted that efforts including those of Olson et al. [34] and Desjardins et al. [35] have proposed modified Level Set methods to deal with this problem. Tryggvason gathered a comprehensive history of VOF and Level Set methods in his book [4].

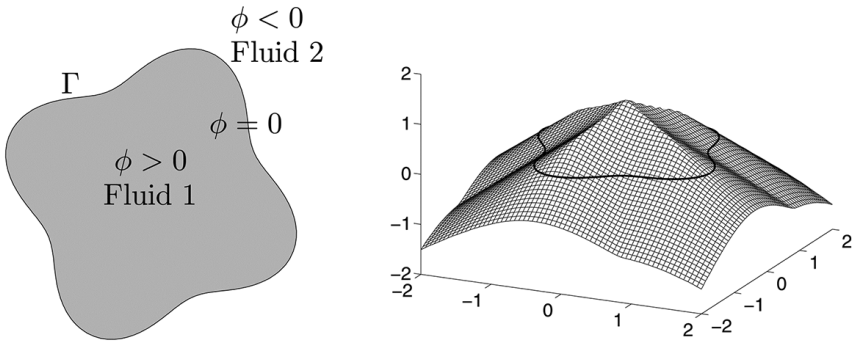

Figure 2.2: Distance function distribution in the LS method.

2.1.3 Coupled LS/VOF method

n order to take advantage of the benefits of both methods, i.e. the mass conservation of VOF and the smooth interface description of LS, Bourlioux [11] proposed the Coupled Level Set-VOF-(CLSVOF) method. In fact, the implementation of CLSVOF by Sussman and Puckett [36] made it a popular method in two-phase flow simulation. Later, researchers extended this promising method for different applications [37, 38].

Most of CLSVOF methods use two-way coupling by advection of both functions (VOF and LS), where geometrical advection algorithms are employed. However, these accurate methods

have significant complexity and are computationally expensive compared to basic VOF and Level Set methods [35]. Kunkelmann and Stephan [41] coupled the arithmetic VOF (in the OpenFoam framework) with the Level Set in one-way approach and simulated boiling bubbles due to evaporation. They initialized the distance function from the advected volume fraction in order to calculate the interface curvature/surface tension force. Next, Albadawi et al. [42] extended this method, namely Simple Coupled Level Set-VOF (S-CLSVOF), to study bubble growth physics. The S-CLSVOF method showed promising result, however was not capable for every case.

2.1.4 Interfacial forces implementation methods

There are several challenges arising in the numerical simulation of two-phase flows, in particular, in the determination of the interface topology and handling the stresses and material discontinuities at the phase boundary. Modeling the interfacial forces (surface tension, buoyancy and viscous) plays a determining role in the accuracy of two-phase flow simulation. Two different approaches have been widely used to represent surface tension effect, namely the continuum surface force and the ghost fluid method. These methods outline the placement and distribution of the capillary force in the interfacial region and are agnostic to the choice of curvature computation method. In the CSF model proposed by Brackbill et al. [24], the surface tension force appears as a diffuse body force, while the material properties are averaged across the interface. As a result, the distributed body force in the momentum equation can lead to the onset of physically unrealistic velocities orders of magnitude greater than the characteristic velocities of the simulation. GFM [39], on the

other hand, is a technique utilized to handle sharp transitions, shocks, material properties etc. In the case of capillary forces, GFM explicitly introduces the singular pressure jump condition into the discretization equations while material discontinuities are accounted for automatically. Each phase is artificially extended across the interface, producing ghost cells which contain properties of the extrapolated phase used for the discretization scheme, removing the tendency for the adjacent interfacial cells to diffuse due to the sharp transition. The capability to enforce continuity is not influenced using GFM here, i.e. should the flow be incompressible, the same rules apply regarding the projection method used to split the pressure-velocity coupling as the only modifications proposed here deal with a redistribution of forces, not modification to the governing principles.

The GFM first introduced by Fedkiw et al. [39] to capture sharp density discontinuities for a compressible solver, later extended to incorporate the Level-Set method (LS/GFM) to solve sharp deflagration and detonation discontinuities [40]. Liu et al. [41] developed GFM as a boundary condition method to solve variable coefficient Poisson equation. For incompressible laminar two-phase flow, first Kang et al. [42] extended GFM to account for the pressure jump caused by normal viscous stresses at the interface. Later Huang et al. [43] implemented surface tension using GFM for interface tracking on curvilinear grids. Sussman et al. [44] introduced the Sharp interface method based on GFM to speed up the CLSVOF solver. Desjardins et al. [35] incorporated GFM to the conservative level set methodology [34], while neglecting viscous discontinuities. Later, Desjardins and Moureau [35] extended their method by decoupling velocities at interface to capture high density ratio flows. Aanjaneya et al. [45] developed an approach for the implicit coupling of incompressible liquid with compressible gas solutions by using GFM, allowing for

compressibility effects to influence bubble volume without the need to model full compressibility. For the viscous discontinuities, Hayashi and Tomiyama [46], and Lalaane [47], presented a GFM discretization of the viscous term in comparison with CSF method. While all the mentioned works has been applied using the finite difference framework and various projection methods for the mass/momentum solutions, Vukevi et al. [48] utilized GFM to treat the hydrostatic force based on finite volume method for large-scale flows where interfacial viscous and capillary forces are less significant.

2.2 Buoyant oil jet in water cross flow

In this section, first we briefly review the previous studies on deep sea oil spill which are mostly large scale mathematical models and experiments. Then, we explore publications on buoyant jets including numerical simulation and experimental studies of cross-flow oil jets.

2.2.1 Deep sea oil spill

Concerning the declining onshore reserves of oil/gas, worldwide exploration operations are moved toward offshore oil/gas sources, which recently are taking place at deeper locations in the ocean. This offshore deep water production substantially increase environmental concerns on the potential of accidental releases from well blowouts. The public awareness of the disastrous damages of oil spills on the environment has put pressure on big oil companies to be prepare for such possible

accidents. Thus, in the recent decade, researchers have conducted researches to understand the oil spill hydrodynamics. For the OS plume, integral models have been utilized extensively, which can be classified into two types of Eulerian and Lagrangian approaches. Yapa and Zheng [45] gathered a comprehensive review on integral models used for buoyant jet/plume simulation. Fundamental works on Eulerian integral model, which works based on a set of spatially fixed control volumes, can be found in the publications by Hirst [46] and Schatzmann [47].

Hirst introduced a new integral method to predict the hydrodynamic and thermal behavior of the buoyant jets injected into stratified ambients. Hirst [46] utilized a generalized entrainment function to include the effects of internal turbulence and the cross flow. Schatzmann [47] mathematically predicted the spreading and rising of a subsurface jets discharged into a stratified, flowing ambient fluid. In the Lagrangian integral models, the buoyant jets are solved by a series of isolated moving elements [48]. Basic exemplary Lagrangian integral models can be found in papers by Frick [49] and Lee and Cheung [48]. Frick developed a 2D Lagrangian integral model for a buoyant jet to predict the trajectory, dispersion of the buoyant jet [49]. Lee and Cheung [48] proposed a model (JETLAG model) for a general buoyant jet with three-dimensional trajectory with uni-directional ambient flow. Johansen et al. (at SINTEF applied chemistry, Norway) [59] conducted a real deep water oil/gas release experiment at Norwegian Sea to better understand how oil and gas would behave during a deep blowout and calibrate the numerical models. The liquid was released in 844 m of water in this experiment. They compared experimental data with results predicted by Johansens DeepBlow model. According to their work, DeepBlow model did a reasonable job of

predicting the time to surface and the location of the slick although some tuning were needed for the bubble/droplet sizes, gas dissolution rate, and hydrate formation.

2.2.2 Buoyant oil jets

Considering the deep sea oil spill phenomenon in small scale, oil jet discharges into a crossing liquid medium with various flow and fluid properties. This phenomenon of injection and break up of immiscible liquid jet in another liquid is of fundamental importance in various scientific and industrial liquid-liquid applications. Studies on jet formation and breakup started by experimental and theoretical studies of Meister et al. [49, 50], who aimed to predict the breakup length and the droplet size for a oil jet in quiescent water. Later, Kitamura et al. [51] reported that the linear analysis is not valid for jetting mode of breakup. Subsequently, other researchers [52, 53, 54] modified previous analysis incorporating effects of viscosity and inertia in their models. Also, Song et al. [55] reported qualitative experimental results for drop formation at low Reynolds numbers.

For the buoyant oil jet, several breakup modes are reported as shown schematically in Fig.2.3 [51, 56]. For *Dripping* mode, which happens at low injection velocities, droplets are formed periodically at near field without jet formation. Higher injection velocity result into *jetting* breakup modes (axisymmetric and asymmetric), for which the breakup length increases with the injection velocity. In axisymmetric jetting mode, as injection velocity increases jet reaches its maximum length at the velocity called u_{max}. For this mode, axisymmetric capillary waves are dominant force

to break off droplets from the tip of the jet. For *asymmetric jetting* mode, when velocity is greater than u_{max}, asymmetric instabilities around the jet primarily break up the jet, while the breakup length decreases. The last breakup mode is *atomization*, which occurs at high injection velocities, in which jet breaks up near the nozzle producing ligaments and non-uniform droplets.

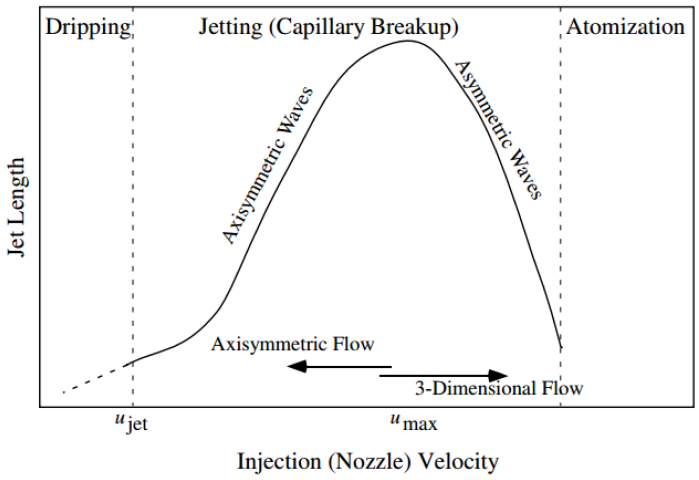

Figure 2.3: Schematic diagram of breakup modes for liquid discharged upward into another liquid medium reported by experimental researchers.

For numerical studies on buoyant oil jet, first Richards et al. [57] used VOF method to study breakup dynamics in axisymmetric domain. Next, Homma et al. [56] studied various breakup modes on buoyant axisymmetric jets. In this study, they used front tracking method and simulation was limited to axisymmetric cases. Subsequently, Lakdawala et al. [58] utilized dual-grid level set method to study droplet formation regimes on buoyant oil jets. They reported various patterns in periodicity droplet formation, while they did not study asymmetric jetting cases.

CHAPTER 3
NUMERICAL METHODOLOGY

In this chapter, we describe numerical methodology developed and implemented for two-phase flow simulation. In the following sections, first the volume of fluid (VOF) methof is described in details. Then, the developed algebraic coupled level set/voluem of fluid (A-CLSVOF) method is introduced. Next, the A-CLSVOF method is equiped with ghost fluid implementation of interfacial forces to have A-CLSVOF/GFM method. Eventual, new version of our solver with called decoupled pressure DP-CLSVOF/GFM is presented.

3.1 Volume of fluid (VOF)

In this section, the base volume of fluid solver on the OpenFOAM framework is outlined. First, governing equations are presented. Then, the algebraic volume fraction advection is described. Next, we present Pressure Implicit with Splitting of Operators (PISO) method to predict pressure and velocity at each time step.

3.1.1 Governing equations

The equations governing an incompressible, immiscible, two-phase flow problem involving VOF advection and momentum equations are as follows:

$$\frac{\partial \alpha}{\partial t} + \nabla.(\alpha \vec{u}) = 0 \tag{3.1}$$

$$\frac{\partial \rho \vec{u}}{\partial t} + \nabla.(\rho \vec{u} \otimes \vec{u}) = -\nabla P_d + \nabla.T^{'} + \vec{g}.\vec{x}\nabla\rho + \sigma\kappa\vec{n}\delta \tag{3.2}$$

Here, $\vec{u}$ is the velocity vector, α the volume fraction step function, ρ is the density, P_d is the dynamic pressure defined as $P_d = P - \rho\vec{g}.\vec{x}$, g the gravitational acceleration, σ surface tension coefficient, κ interface curvature, $\delta(x - x_s)$ interface Dirac delta function, and $\vec{n}$ the interface normal. The body force includes gravitational and surface tension forces converted to volume forces. The viscous stress tensor reads:

$$T^{'} = \mu\left(\nabla\vec{u} + (\nabla\vec{u})^T\right) \tag{3.3}$$

then the viscous term is rewritten as:

$$\nabla.T^{'} = \nabla.(\mu\nabla\vec{u}) + \nabla\vec{u}.\nabla\mu \tag{3.4}$$

The solver treats the phases as a mixture where material properties are averaged across the interface using the volume fraction of the liquid composition in each cell. The updated physical properties (density and viscosity or any other material property dependent on phase composition) in the domain are interpolated using current volume fraction as follows.

$$\rho(\alpha) = \rho_g + (\rho_l - \rho_g)\,\alpha \tag{3.5}$$

$$\mu(\alpha) = \mu_g + (\mu_l - \mu_g)\,\alpha \tag{3.6}$$

where subscripts g and l denote gas and liquid phase respectively.

3.1.2 Volume fraction algebraic advection

As discussed in the literature review (chapter 2), The algebraic advection scheme using a compressive relative velocity is utilized in the model [29]. The advection of the VOF field as shown in Eq. (3.1) results in smearing over interfacial cells since low order convective schemes result in a diffuse, yet bounded solution. Higher order schemes improve accuracy but are infeasible for use with scalar fields including sharp interfaces as the result becomes unstable and unbounded in regions near the interface [59]. To deal with this problem, an artificial compressive flux is added and oriented normal to the interface. The volume fraction advection equation Eq. (3.1) becomes:

$$\frac{\partial \alpha}{\partial t} + \nabla.(\alpha u) + \alpha(1-\alpha)u_r = 0 \tag{3.7}$$

which has a discretized form of:

$$\partial_t \alpha + \sum_{f \in S_i} \frac{1}{v_i} \left(\langle \alpha \rangle_f \phi + \langle \alpha \rangle_f \phi_f \langle 1 - \alpha \rangle_f \phi_f \phi_r \right) = 0, \tag{3.8}$$

Here, is the volume of each cell and volume flux at face of f, while denotes the interpolated face fields. Subscript of r stands for compression term and is calculated as follows:

$$\phi_r = |\phi_c| \langle n_s \rangle_f . S_f, \tag{3.9}$$

$$\phi_c = min\left[c_\alpha \frac{|\phi|}{|S_f|}, max\left(\frac{|\phi|}{|S_f|} \right) \right], \tag{3.10}$$

Further details of advection approach can be found in the references [31].

3.1.3 Surface tension force

The base VOF solver utilizes CSF (Continuum Surface Force) model to present surface tension into momentum equation Eq. (3.2). Based on CSF model, which is widely used in VOF and LS methods, surface tension is converted into a resulting bulk volume force. The magnitude of this force is proportional to the interface curvature and results in a pressure jump across the interface. In order to determine the equivalent volume force, the quantity of interfacial area in every cell must be known. The CSF surface tension force calculates as:

$$F_\sigma = \sigma \kappa n \delta \tag{3.11}$$

where curvature calculates as $\kappa = -\nabla.n$ and Dirac delta function defines as $\delta = |\nabla n|$. Substitution of Eq.3.11 in momentum equation in direction of interface normal $n = \frac{\nabla.n}{|\nabla.n|}$ results into $F_\sigma = \sigma\kappa\nabla\alpha$ for surface tension in momentum equation Eq. 3.2.

3.1.4 Pressure Implicit with Splitting of Operators

According to the finite volume approach, the volume integral discretization of the momentum equation (Eq.2) appears as [60]:

$$\begin{gathered}\int_{\Omega_i} \frac{\partial \rho u}{\partial t} dV + \int_{\partial\Omega_i} (\rho uu).nds = -\int_{\Omega_i} \nabla.P_d dV - \int_{\Omega_i} g.x\nabla\rho dV + \\ \int_{\Omega_i} \sigma\kappa\nabla\alpha dV + \int_{\partial\Omega_i} (\mu\nabla u).nds + \int_{\Omega_i} \nabla u.\nabla\mu dV\end{gathered} \tag{3.12}$$

The PISO method for the iterative solution of the NS equations consists of two primary steps, a predictor and a corrector of the velocity and pressure field. The momentum predictor occurs before entering the iterative loop and solves the NS for based on the velocity $\vec{u}^n$ and pressure P_d^n at the previous time step. The convective term is linearized with $\vec{u}^n$, and P_d^n allows for an implicit solution of the predicted velocity which does not yet satisfy continuity.

$$A_P u_P^\star + H(u_N) = -\nabla P_d^n + \sigma\kappa\nabla\alpha^{n+1} - g.x\nabla\rho^{n+1} \tag{3.13}$$

The discretization of the temporal, convection and diffusion terms results in the velocity coefficient matrix, $A_p + H^{'}(\vec{u}_N$. Where A_p and $H^{'}(\vec{u}_N)$ are diagonal and off-diagonal coefficient matrices. The subscripts P and N denote the considered control volume and its neighbors respectively. With a predicted velocity, $\vec{u}^\star$, Eq.3.14 may be reconstructed to define the first corrected pressure and velocity, $P_d^\star$ and $\vec{u}^{\star\star}$. By introducing $H = \vec{g} - H^{'}(\vec{u}^\star)$, the dynamic pressure is accounted for by the explicit source term in Eq. 3.14. The old time values are replaced by the predicted values and $\vec{u}_p^{\star\star}$ is discretized explicitly.

$$u_P^{\star\star} = A_P^{-1}\left[H(u_N^\star) - \left(\nabla\, P_d^\star - \left(\sigma\kappa\nabla\alpha^{n+1} - g.x\nabla\rho^{n+1}\right)\right)\right] \tag{3.14}$$

Since $\vec{u}^{\star\star}$ is determined explicitly in this step, the corrected pressure, $P_d^\star$, may be determined implicitly by imposing the continuity condition,

$$\nabla.\left[A_P^{-1}(\nabla P_d^\star)\right] = \nabla.[A_P^{-1}\left(H(u_N^\star)\right] + \nabla.\left(\sigma\kappa\nabla\alpha^{n+1} - g.x\nabla\rho^{n+1}\right) \tag{3.15}$$

Finally, the corrected velocity, $\vec{u}^{\star\star}$ may be determined according to Eq.3.15 using the corrected pressure from Eq.3.16 [31]. Since face fluxes of velocity/volume are the conserved quantity, the

face fluxes ϕ are constructed from a face interpolated form of Eq.3.15.

$$\phi^{n+1} = A_P^{-1}[H(u_N^{\star})].s_f - A_P^{-1}\left(\nabla P_d^{\star} - \left(\sigma\kappa\nabla\alpha^{n+1} - g.x\nabla\rho^{n+1}\right)\right).s_f \tag{3.16}$$

Here, S_f is the area vector of a cell face and $\phi_f = \vec{u}_f.S_f$ is the corresponding volume flux at a face. This process may be repeated from Eq.3.15 until sufficient convergence is met.

3.1.5 VOF algorithm

At each time step, following calculations perform (Fig. 3.1):

1. Volume fraction field is advected to get α^{n+1} using Eq.(3.8).

2. Material properties, density and viscosity update according to new volume fraction Eq.(3.5,3.6).

3. Interface normal, curvature and accordingly surface tension force are calculated and substitute in momentum equation.

4. The iterative PISO loop solution is performed to have new velocity and pressure.

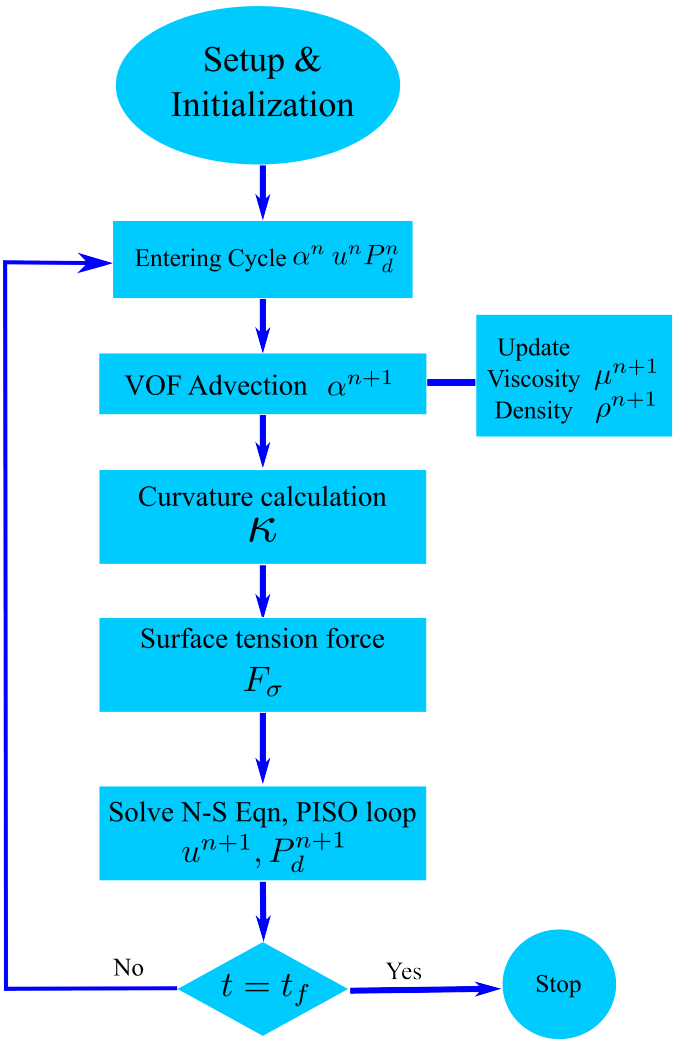

Figure 3.1: Flow diagram of VOF method for one computational cycle.

3.2 Algebraic coupled level set/volume of fluid

In the following sections, the Algebraic-Coupled Level Set-Volume of Fluid (A-CLSVOF) method is described in details. The base VOF solver on the OpenFoam framework is outlined, and the

coupling technique is illustrated in the following. First, we present the theoretical formulation of the A-CLSVOF method and its implementation in the Navier-Stokes equations. As an overview, the volume flux/velocity field is used to advect the VOF field, resulting in a mass conservative movement of the interface. Material properties are updated based on the mixture volume fraction. The LS field is then advected (or initialized from seed points at the interface if t=0) and the cells containing an interface contour ($\alpha = 0.5$) are updated from the new mass conservative VOF field and serve as the seed points for the reinitialization procedure. The reinitialization continues until steady state is reached and interface curvature is computed from calculations on the new LS field identifying the normal-orientation of the interface. It should be noted that adding compressibility, thermal effects on surface tension coefficients, density etc. or even phase change adds complexity to the proposed model, but in no way invalidates the modifications proposed here.

3.2.1 Governing equation

The equations governing an incompressible, immiscible, two-phase flow problem involving LS redistancing include VOF advection Eq.(3.1), momentum Eq. (3.2) and LS distance function advection as follows:

$$\frac{\partial \psi}{\partial t} + \nabla.(\psi \vec{u}) = 0 \tag{3.17}$$

In the A-CLSVOF we have a one-way coupling approach where the interface position is determined according to volume fraction function converted into distance function. The LS function is advected to expedite the simulation by providing an initial guess for the to-be-reinitialized distance

field. The distance function is discretized as follows:

$$\partial_t \psi + \sum_{f \in S_i} \frac{1}{v_i} \left(\langle \psi \rangle_f \phi \right) = 0, \tag{3.18}$$

3.2.2 Coupling VOF and LS method

After the advection of volume fraction and distance function (Eq. 3.1 and 3.18), the advected distance function, ψ^{n+1}, becomes ψ_0^{n+1} and is updated at interfacial cells ($0 < \psi < 1$) by converting from the volume fraction (Eq. 3.20) to ensure mass conservation. The interface position of iso-line $\alpha = 0.5$ converts into iso-line $\psi = 0$ for the distance function in the Level Set field at the fluid interface, while ψ takes positive and negative values in the liquid and gas phase respectively. The initial distance function at transition region ψ_0^{n+1} derives from ψ^{n+1} as:

$$\psi_0^0 = (2\alpha^0 - 1).\Gamma \tag{3.19}$$

Where Γ represents a distance parameter which is defined by domain grid size as $\Gamma = C_\Gamma \Delta x$. Generally, the distance parameter Γ and interface thickness $\varepsilon = C_\varepsilon \Delta x$ should be consistent, i.e.$C_\varepsilon = 2C_\Gamma$. The interface thickness ε determines the sharpness of transition region between two fluids. Typically in our simulation the coefficients are set as $C_\varepsilon = 2C_\Gamma = 1.4$ as these values consistently yielded a stable and accurate result.

3.2.2.1 Reinitialization

After updating the advected LS field at the interfacial cells, ψ_0^{n+1} requires reinitialization in order to redistance the field in regions near the interface that became skewed during advection. This is an iterative process that occurs over artificial time, τ , in order to correct the distance function for every cell. The reinitialization methods are computationally expensive but play a determining role for overall accuracy and efficiency of the model in the computation of interface curvature and subsequently surface tension force [**?**, **?**]. Initially, Sussman introduced distancing procedure which required the iterative solution of a PDE until a fully distanced LS field, , was reached [**?**]:

$$\psi_\tau + S(\psi)(|\nabla\psi| - 1) = 0 \tag{3.20}$$

Where ψ_τ, $S(\psi)$, and $(|\nabla\psi| - 1)$ are the temporal derivative over an artificial time, τ, a sign function (described below) and a quantity that defines the initialization error. In the S-CLSVOF method, authors solved the Eq.(3.21) with $S(\psi_0) = \psi_0/|\psi_0|$ for a fixed number of iteration as $n_{corr} = \varepsilon/\Delta\tau$, where the artificial time step was set for stability at $\Delta\tau$ [61]. As we show in the following, its solution does not guarantee the correct value of the distance function, especially for cells around the interface and also those undergoing topological changes. This was likely attributed to two factors, the form of $S(\psi_0)$ where cells at the interface are free to change for the entire duration of the reinitialization procedure, long after convergence had been met, and the discretization of the quantity $|\nabla\psi|$ in Eq. (3.21). To deal with these problems we employed the use of the Hamilton Godunov function [**?**], and second order accurate temporal and spatial $(O\Delta\tau^2, O\Delta x^2)$ discretization schemes [**?**] for the evaluation ψ_τ and $|\nabla\psi|$ respectively. The form of

Eq.(3.21) can be modified by the Hamilton Godunov (G) function:

$$\psi_\tau + S(\psi,\psi_0)\left(G(D_\zeta^+\psi, D_\zeta^-) - 1\right) = 0, \quad \zeta = x,y,z \tag{3.21}$$

Where, $S(\psi,\psi_0)$ is the smoothed sign function and formulated as proposed by Peng et al. [**?**]:

$$S(\psi,\psi_0) = \frac{\psi_0}{\sqrt{\psi_0^2 + |\nabla\psi^\tau|^2\Delta x^2}} \tag{3.22}$$

The sign function used in this model can be described as an initialization controller where the artificial time step is scaled in regions near the interface when the distance function begins to converge. $S(\psi,\psi_0)$ serves three primary functions 1. ensuring the incremental changes to $\psi^{\tau+1}$ be either positive or negative, hence the name sign function, 2. under relaxing the incremental changes to $\psi^{\tau+1}$ near the interface resulting from the addition of Δx^2 and finally, 3. allowing the interfacial cells to converge quickly in the first few iterations when $|\nabla\psi| < 1$, and when $|\nabla\psi| \to 1$, Δx^2 (described above) then contributes to under relaxation of the interfacial cells.

Next, we will discuss the second order accurate discretization of the gradients of ψ during reinitialization. The x-direction upwind and downwind differencing expressions are defined as:

$$D_x^+\psi_i = \frac{\psi_{i+1} - \psi_i}{\Delta x} - \frac{\Delta x}{2} minmod(D_x\psi_i, D_{xx}\psi_{i+1}), \tag{3.23}$$

$$D_x^-\psi_i = \frac{\psi_i - \psi_{i-1}}{\Delta x} - \frac{\Delta x}{2} minmod(D_{xx}\psi_i, D_{xx}\psi_{i-1}). \tag{3.24}$$

Here $D_\zeta^\pm\psi$ is a 2nd order accurate, one-sided (upwind or downwind) approximation of the first derivative along the three principle axes, represented by ζ. $D_{xx}\psi_i = (\psi_{i-1} - 2\psi_i + \psi_{i+1})/\Delta x^2$ is the discretization for a second order central difference of ψ_i in the x direction ($\psi_x x$). The minmod function returns zero value for the argument with different sign, while gives back the argument

with smaller absolute value when they have same sign. This feature enables the reinitialization procedure to control when using second order upwinding is appropriate and for which cells. As the initialization procedure begins, the width of the transition region of the interface is small enough that a second order scheme for a cell in the liquid phase may reach across the zero level set into the gas phase where that cell (or neighboring cells) has yet to converge. The concavity to the field in this situation, identified by the sign of the second derivative, would indicate that there is indeed a sign change between the arguments of minmod() in Eqs.(3.24 and 3.25), resulting in a zero value. When the advancing front is a sufficient distance from the opposite front, then the arguments of minmod() will possess the same sign and would therefore return the lesser of the two arguments, namely, the upwind direction second derivative, making Eqs.(3.24 and 3.25) second order accurate. The Hamiltonian Godunov function for the liquid (G_+) and the gas phase (G_-) of the distance function are defined as:

$$G_+(a_\zeta, b_\zeta) = \sqrt{max(a_{x,-}^2, b_{x,+}^2) + max(a_{y,-}^2, b_{y,+}^2) + max(a_{z,-}^2, b_{z,+}^2)} \tag{3.25}$$

$$G_-(a_\zeta, b_\zeta) = \sqrt{max(a_{x,+}^2, b_{x,-}^2) + max(a_{y,+}^2, b_{y,-}^2) + max(a_{z,+}^2, b_{z,-}^2)} \tag{3.26}$$

Where $a_{\zeta,+} = max(a_\zeta, 0)$ and $a_{\zeta,-} = min(a_\zeta, 0)$. The respective vector fields, a and b store the upwind and downwind gradients of ψ with respect to the principle coordinate axes. The Gudonov function can finally be defined as a means of determining the upwinding direction for $\nabla\psi$ based on the global coordinate system and the orientation of the constantly changing ψ. In our method, we use the volume fraction, α, to weight each component, (G_+) and (G_-), of the new distance function after each iteration. Since (G_+) and (G_-) are computed over the entire domain, the volume fraction of each cell is used for volume-fraction-weighting (similar to Eqs.3.5 and 3.6)

the combined results of the Godunov functions. This helps to ensure corrections for ψ over the artificial time come primarily from the component of $(G_{+/-})$ that was discretized to operate in that portion of the domain. This has shown an improvement in the orientation of the converged zero-level-set with respect to the orientation of the mass conservative volume fraction field. The resulting first order accurate $(O\Delta\tau)$ expression for the distance function at the next artificial time step, $\psi^{\tau+1}$ (Eqs.3.28,3.29,3.30 only), and its constituents are as follows:

$$\hat{\psi}_{+}^{\tau+1} = \psi^{\tau} - \Delta\tau.S(\psi^{\tau},\psi_0)\left(G_{+}(D_{\zeta}^{+}\psi^{\tau}, D_{\zeta}^{-}\phi^{\tau}) - 1\right) \tag{3.27}$$

$$\hat{\psi}_{-}^{\tau+1} = \psi^{\tau} - \Delta\tau.S(\psi^{\tau},\psi_0)\left(G_{-}(D_{\zeta}^{+}\psi^{\tau}, D_{\zeta}^{-}\phi^{\tau}) - 1\right) \tag{3.28}$$

$$\hat{\psi}^{\tau+1} = \alpha\hat{\psi}_{+}^{\tau+1} + (1-\alpha)\hat{\psi}_{-}^{\tau+1} \tag{3.29}$$

The implementation of the second order accurate temporal discretization $(O\Delta\tau^2)$ then proceeds by following Shu and Osher [34], where the term $\hat{\psi}_{+/-}^{\tau+1}$ now denotes a temporary solution used to comprise the second order accurate result shown below.

$$\psi^{\tau+1} = \frac{\psi^{\tau} + \hat{\psi}^{\tau+2}}{2} \tag{3.30}$$

Where $\psi^{\tau+1}$ above is the result at the next artificial time. The temporary solution for $\hat{\psi}^{\tau+2}$ then proceeds as before:

$$\hat{\psi}_{+}^{\tau+2} = \hat{\psi}_{+}^{\tau+1} - \Delta\tau.S(\hat{\psi}^{\tau+1},\psi_0)\left(G_{+}(D_{\zeta}^{+}\hat{\psi}^{\tau+1}, D_{\zeta}^{-}\hat{\psi}^{\tau+1}) - 1\right) \tag{3.31}$$

$$\hat{\psi}_{-}^{\tau+2} = \hat{\psi}_{-}^{\tau+1} - \Delta\tau.S(\hat{\psi}^{\tau+1},\psi_0)\left(G_{-}(D_{\zeta}^{+}\hat{\psi}^{\tau+1}, D_{\zeta}^{-}\hat{\psi}^{\tau+1}) - 1\right) \tag{3.32}$$

$$\hat{\psi}^{\tau+2} = \alpha \hat{\psi}_{+}^{\tau+2} + (1-\alpha)\hat{\psi}_{-}^{\tau+2} \tag{3.33}$$

It should be noted that for the first order accurate result in Eqs.21-23, the hat on $\hat{\psi}$is removed.

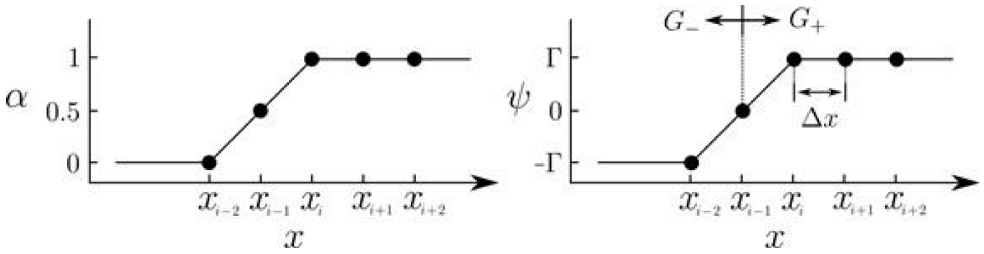

Figure 3.2: 1D discretization of volume fraction (left) and the distance function calculated by Eq.3.34 (right).

Our method, A-CLSVOF is compared with the one presented in S-CLSVOF [61] for the case of two adjacent circular droplets. As illustrated in the Fig.3.3, our approach (left) fully converges over the entire domain, even for the region separating the drops where the upwinding direction for the gradients of the distance function must be chosen carefully. When testing our code in a configuration that does not implement any special discretization scheme or sign function to be consistent with what was presented in [61], we a found a result that suggested incompatibility with common topological change problems including coalescence and break-up. The result on the right of Fig.3.3 was generated by a lower number of iterations over the same increment of $\Delta\tau$ used in our method; this was required due to the formation of a peak in ψ separating the interface as the gradient discretization was drawing data from both interfaces, and not the proper upwinding direction. In any case, the steady state error was calculated at the converged artificial time and before the onset of instability in the method of [61] in an attempt to minimize the error in the

S-CLSVOF method. The error is calculated only in the interfacial region in order to better assess the performance of the semi-converged S-CLSVOF result ($Error = \iiint (|\nabla\psi| - 1)dV / \iiint dV$). Our method indicates an average deviation in $|\nabla\psi|$ from unity of less than 1% when compared to S-CLSVOF averaging 31%.

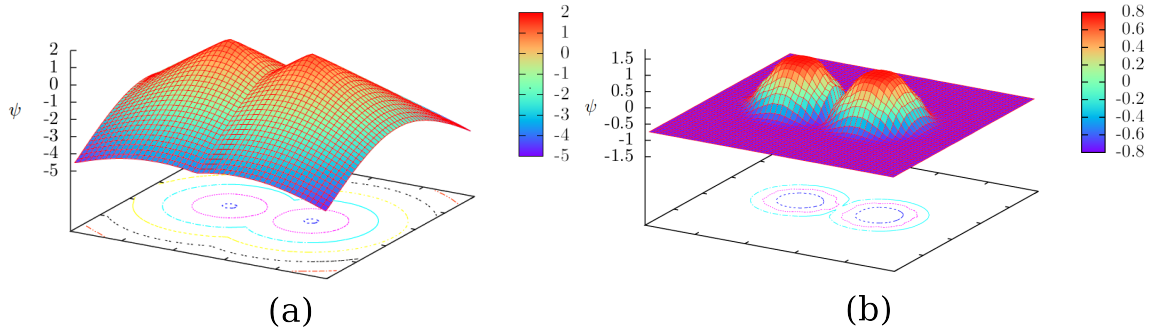

Figure 3.3: Comparison of the reinitialization methods (a) this study: A-CLSVOF, and (b) S-CLSVOF

3.2.3 Curvature calculation

After the new LS field has been reinitialization using the technique described above, the parameters comprising the surface tension force can be updated for use in the momentum equation. Since the magnitude of distance function defines the closest, normal distance to any interface, its gradient naturally aligns orthogonally with the interface, making it the primary candidate for the description of interface topology.

Generally in the VOF method, the interface normal is defined as $n_s = \frac{\nabla\alpha}{|\nabla\alpha|}$, and is based on average volume content in a given cell, i.e. the actual interface orientation is inferred by a rough estimate of the spatial variations in the volume fraction field from cell to cell. Though field operations on α may seem to be valid in determining the interface curvature due to its mass conservative properties and its role in determining the phase composition, α fails to approximate the sub-grid curvature of an interface that is smooth and continuous. α possesses inconsistent variations along the interfacial region that align with mesh features. For example, standard second order linear face interpolation of α neglects the contribution of neighboring cells that share vertices but no face with the current cell where n_s is being calculated, meaning these adjacent cells never see the effects of one another. These cells can communicate in other ways, e.g. weighted averaging or pure inverse distance interpolation. Raeini et al. [**?**] proposed that the cells can spread data through multiple interpolations of cell centered values to cell faces and relaxing the reconstructed result by blending the new reconstructed center value with the original with some arbitrarily chosen relaxation constant. Though this procedure is equipped to smooth the variations in α by producing somewhat diffuse LS like region, this mode of data transfer is missing theoretical foundation.

In this study, the use of the LS field is used to establish the orientation of the interface. Since we understand that operations on field variables on structured, orthogonal grids fail to account for all adjacent cells for standard, robust discretizations, we tested the increase in accuracy when using $n_s(\psi)$ compared to an interface normal built from the inverse-distance-weighted point interpolation of the former, $\hat{n}_s(n_s(\psi))$. The procedure is defined below:

1.) Calculate the basic interface normal vector at each cell center by:

$$n_s = \frac{\Delta\psi}{|\Delta\psi|} \tag{3.34}$$

2.) Averaging local cell center normals to cell vertices (points) by:

$$n_s^p = \frac{\sum_{m\in N_i}\left(n_s^m |d_{\overline{im}}|^{-1}\right)}{\sum_{m\in N_i}|d_{\overline{im}}|^{-1}} \tag{3.35}$$

where m indexes through the neighboring cells of point i who share common vertices, N_i is the total number of neighboring cells and $|d_{\overline{im}}|$ is the distance from the coordinates of point i to the center-of-volume of cell m.

3.) Finally, we define the new normal at the cell center from the inverse-distance-weighted average of the cells constituent points:

$$\hat{n}_s' = \frac{\sum_{p\in N_p}\left(n_p^s |d_{\overline{cp}}|^{-1}\right)}{\sum_{m\in N_p}|d_{\overline{cp}}|^{-1}} \tag{3.36}$$

where p indexes through the vertices forming a given cell, N_p is the total number of constituent cell vertices and $|d_{\overline{cp}}|$ is the distance from cell center c to the vertex at point p.

4.) Finally the interface normal is re-normalized to ensure it remains a unit normal vector:

$$\hat{n}_s = \frac{\hat{n}_s'}{|\hat{n}_s'|} \tag{3.37}$$

This method transfers data by means of inverse-distance-weighting and does not rely on the spread of data through multiple iterations and blending factors. Since the interface curvature is to be free of sharp discontinuities, variations in the orientation of the interface normals along the interface should also be smooth and continuous. Since the LS field is reinitialized from cells containing

$0 < \alpha < 1$, it is anticipated that initially, some cells may be poorly conditioned and may not converge as quickly or as absolutely as neighboring cells. Since the above normal filtering method spreads the data locally where there is little variation in the normal from cell to cell, and that most cells have a relatively symmetric distribution of points surrounding the center, changes to the interface normal will be either 1. unperceivable in regions where there is smooth and free of many sharp transitions or 2. will adjust the direction of the corrected normal to be more consistent with its neighbors along the interface. This minimizes the amount of abrupt or discontinuous behavior of interface normal orientation along the interface, and has demonstrated an increase in accuracy when calculating interface curvature. Once the interface normal vectors are calculated and updated, the interface curvature can be computed using the Gauss divergence theorem as:

$$\kappa = \nabla.\hat{n}_s = \sum_f \frac{1}{v_i} S_{f,i}.\langle \hat{n}_{s,i} \rangle_f \tag{3.38}$$

Where v_i and $S_{f,i}$ are volume and faces of cell i where f indexes through all of the faces comprising cell i. As a test case, a droplet was initialized using a coarse representation of the interface, i.e. there was no interfacial transition region, only pure liquid and pure gas. In Table 3.1, we compared the standard normal calculation based on $\nabla.n_s^\alpha$, $\nabla.n_s^\psi$ and finally the smoothed calculation based on $\nabla.\hat{n}_s^\alpha$ for a droplet with a known curvature value of $40m^{-1}$. The table shows the integrated mean of curvature and standard deviation for cells containing the interface region $(0 < \alpha < 1)$ for each configuration. According to the results, our averaging technique provides the best prediction of a sub-grid interface curvature. Observation of the standard deviations illustrates how erratic the calculations of curvature can be when using to describe the interface orientation and also the

additional improvement in the cell-to-cell variation of the interface normal orientation with the filtering routine described above for $\nabla.\hat{n}_s^{\alpha}$.

Table 3.1: Comparison of different curvature values using three different normal calculations for a droplet with a curvature of $40m^{-1}$.

Curvature	$\nabla.n_s^{\alpha}$	$\nabla.n_s^{\psi}$	$\nabla.\hat{n}_s^{\alpha}$
Average curvature	35.14	40.56	40.1
Error	12.1%	1.4%	0.2%
Standard deviation	5.55	14.4	1.45

3.2.4 surface tension force

As been discussed in section 3.1.3, CSF technique is used to implement surface tension force Eq.3.11. If we consider the Eq.3.11 as:

$$F_{\sigma} = \sigma\kappa\lambda \tag{3.39}$$

where indicator field was $\lambda = n\delta(\alpha)$ for VOF method based on volume fraction field. The indicator field quantifies the interfacial area per unit volume for a given cell. It can be shown that $\iiint |\nabla\alpha| dV = \iint dS$, or the integral over a region containing an interface returns the area of the interface enclosed within the integral [**?**]. The indicator field can be defined in many ways; typically, we find $\lambda = \nabla\alpha$ (VOF), and also an implementation using the smooth distance function $\lambda = \delta(\psi)\nabla\psi$ or $\lambda = \delta H$. Here, $\delta(\psi)$ is Dirac function Eq.(4.4) determining narrow region around

interface for surface tension force and H is Heaviside function Eq.(4.5) which generally used for smoothing discontinuous properties over the interface in a manner consistent with Eq.(3.5). The last two expression are mathematically equivalent $\delta(\psi)\nabla\psi = \nabla H$, however the numerical implementation causes some discrepancies in the final result.

$$\delta(\psi) = \begin{cases} 0 & |\psi| > \varepsilon \\ \frac{1}{2\varepsilon}\left(1 + cos\frac{\pi\psi}{\varepsilon}\right) & |\psi| \leq \varepsilon \end{cases} \tag{3.40}$$

$$H(\psi) = \begin{cases} 0 & \psi < -\varepsilon \\ \frac{1}{2}\left[1 + \frac{\psi}{\varepsilon} - \frac{1}{\pi}sin\frac{\pi\psi}{\varepsilon}\right] & |\psi| \leq \varepsilon \\ 1 & \psi > \varepsilon \end{cases} \tag{3.41}$$

In the Table 3.2, we compare the three indicator fields noted above for the case of a static droplet with a known total interfacial area. Table 3.2 presents the error for the field operation $A_s = \iiint |\lambda| dV$ compared to the analytical solution for the external area of a hollow cylinder with a known internal volume. It is evident that the error from using the Heaviside function as the indicator field, λ, is lower than the other two fields and is substantially lower when considering the coarse grid.

Table 3.2: Comparison of error for the indicator field, λ using three methods.

Grid/Indicator fields	$\nabla\alpha$	$\delta(\psi)\nabla\psi$	∇H
100-100	0.99%	2.4%	0.2%
300-300	1.02%	0.08%	0.06%

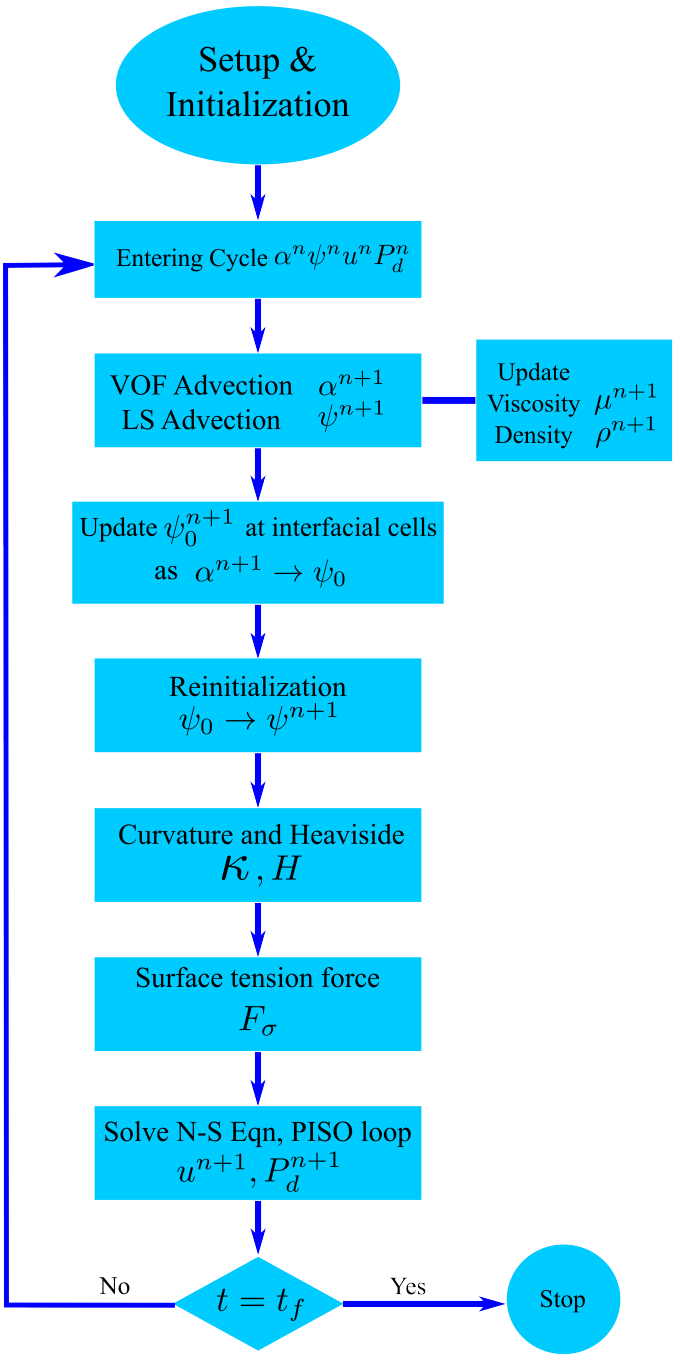

Figure 3.4: Flow diagram of A-CLSVOF method for one computational cycle.

Combining all of the above computations and filtering yields a set of fields that take a coarse, approximate representation of the phase fields, and produces a smooth and more continuous representation of an interface that would exist on a sub-grid scale. Once the refined interface orientation is established, the surface tension force defined in Eq.(3.11) is then used as a CSF source term in Eq.(3.2 which is then recast and coupled with the continuity equation, resulting in a capillary flux which modifies the flow field.

3.3 Ghost fluid method

In this section, we present the theoretical implementation of the surface tension, hydrostatic and viscous forces using the GFM in the incompressible NS equations. We apply the GFM finite volume discretization to the A-CLSVOF method [**?**] with the PISO (Pressure Implicit with Splitting of Operator) solution [**?**] of the momentum equations. In the next section, we drive the two-phase incompressible NS equation with corresponding interfacial jump conditions.

3.3.1 Governing equation

The continuity and momentum equations for an incompressible two-phase flow have the following form [35]:

$$\frac{\partial \vec{u}}{\partial t} + \nabla.(\vec{u} \otimes \vec{u}) = -\frac{\nabla P}{\rho} + \frac{1}{\rho}\nabla.\left(\mu\left[\nabla u + \nabla u^T\right]\right) + \vec{g} + \frac{1}{\rho}\sigma\kappa\vec{n}\delta_\Gamma \tag{3.42}$$

Decomposing the pressure into dynamic and hydrostatic parts as $¶_d = P - \rho\vec{g}.\vec{x}$, and considering $\left(\mu\left[\nabla u + \nabla u^T\right]\right) = \nabla.(\mu\nabla u) + \nabla\mu.\nabla^T u$, N-S equations reads:

$$\frac{\partial\vec{u}}{\partial t} + \nabla.(\vec{u}\otimes\vec{u}) - \nabla.(\nu\nabla\vec{u}) = -\frac{\nabla P}{\rho} + \frac{1}{\rho}\nabla.\left(\mu\left[\nabla u + \nabla u^T\right]\right) + \vec{g} + \frac{1}{\rho}\sigma\kappa\vec{n}\delta_\Gamma \tag{3.43}$$

Note that the dynamic pressure P_d is used to simplify pressure boundary conditions and that the normal viscous stress term, $\nabla\mu.\nabla^T u$ will be added to the GFM discretization in the pressure Poisson equation. By considering Eq.2 for the pure phases straddling the interface, where velocity is necessarily continuous due to incompressibility, a jump expression for the pressure gradient may be defined and simplified to show the dynamic pressure jump condition:

$$[P_d]_\Gamma = \sigma\kappa - [\rho]_\Gamma g.x + [\mu]_\Gamma n^T.\nabla u.n \tag{3.44}$$

since $[u]_\Gamma = 0$, $\nabla\rho = [\rho]_\Gamma n\delta_\Gamma$, and $\nabla\mu = [\mu]_\Gamma n\delta_\Gamma$. Here $[]_\Gamma$ represents the jump condition of a quantity at the interface, e.g. $[P_d]_\Gamma = P_d^l - P_d^g$. We want to impose the appropriate pressure jump condition at the interface, Lalanne et al. [13] mathematically verified that source terms in the pressure Poisson equation can achieve this while the continuous phases remain unmodified in the momentum solution. Since the pressure jump conditions are to be imposed directly in the pressure Poisson equation, the momentum equation and the corresponding jump conditions to be solved are:

$$\frac{\partial u}{\partial t} + \nabla.(u\otimes u) - \nabla.(\nu\nabla u) = -\frac{\nabla P_d}{\rho} \tag{3.45}$$

$$[P_d]_\Gamma = \sigma\kappa - [\rho]_\Gamma g.x + [\mu]_\Gamma\frac{\partial u_n}{\partial n} \tag{3.46}$$

where $n^T.\nabla u.n = \frac{\partial u_n}{\partial n}$ Note that GFM will be used to discretize the viscous term in Eq.(3.46) to ensure a sharp representation of the viscous stresses and is detailed in the following section. Tra-

ditionally, the jump condition is handled crudely by volume averaging the material properties for interfacial cells (CSF method) with the density in the temporal and convective terms of Eq.(3.44). The singular forces are distributed over the interfacial region, resulting in interfacial forces in the pure-phases that can lead to error and the onset of unphysical velocities. In this study, the one-way coupled Volume of Fluid Level-Set method is used to conservatively track the interface via VOF, and to construct the sub-grid interfacial topology via LS for increased accuracy for the curvature computation. By using GFM with the NS equations in the form of Eq.(3.46) in a modified PISO loop, the implementation of the forces, and the discontinuous density and viscosity are handled directly through the discretization scheme, eliminating the need for averaging. The details of the interface tracking and curvature computations are comprehensively described in section 3.2 with the present discretization and implementation of GFM in the following sections.

3.3.2 GFM-PISO loop

As discussed in section 3.1.4, the PISO method for the iterative solution of the NS equations consists of two primary steps, a predictor and a corrector of the velocity and pressure field. The volume integral discretization of the momentum equation Eq.(3.46) results in the velocity coefficient matrix, $A_p + H(u_N)$ as:

$$A_P u_P^\star + H(u_N) = -\frac{\nabla P_d^n}{\rho} \tag{3.47}$$

and Eqs.(3.15,3.16 and 3.17) respectively convert into:

$$u_P^{\star\star} = A_P^{-1}\left[H(u_N^{\star}) - \frac{1}{\rho}\left(\nabla P_d^{\star} - \left(\sigma\kappa - [\rho]g.x + [\mu]_\Gamma \frac{\partial u_n}{\partial n}\right) n\delta_\Gamma\right)\right] \tag{3.48}$$

$$\nabla.\left[A_P^{-1}\frac{(\nabla P_d^{\star})}{\rho}\right] = \nabla.[A_P^{-1}(H(u_N^{\star})] + \nabla.\left(\frac{\left(\sigma\kappa - [\rho]g.x + [\mu]_\Gamma \frac{\partial u_n}{\partial n}\right) n\delta_\Gamma}{\rho}\right) \tag{3.49}$$

$$\phi^{n+1} = A_P^{-1}[H(u_N^{\star})].s_f - \frac{A_P^{-1}}{\rho}\left(\nabla P_d^{\star} - \left(\sigma\kappa - [\rho]g.x + [\mu]_\Gamma \frac{\partial u_n}{\partial n}\right) n\delta_\Gamma\right).s_f \tag{3.50}$$

As is shown, the jump values only exits at the interface. In the next section, we utilize GFM to discretize momentum predictor and laplacian equation to implement jump conditions.

3.3.3 Ghost fluid method discretization

In this section, we describe the use of GFM for the implementation of the pressure jump condition from Eq.(3.47) in the pressure gradient, Poisson equation, and also the viscous stress term in(Eqs.3.49, 3.50, and 3.46). For the discretization, we follow the GFM approach introduced by Desjardins et al. [35] to estimate the pressure jump for interfacial cells. The pressure gradient and pressure Laplacian in Eqs.(3.48 and 3.49) are where the implementation of the GFM modifies the result for pressure. A linear second order accurate discretization scheme is used for pressure at every cell in the domain, including the interfacial and ghost cells. For a control volume at the

interface, cells in the other phase across the interface are considered to be the ghost cells and contain the pressure jump and gradient information which is extrapolated by a Taylor series expansion across the interface. Finally, the ghost cells relation substitutes into the discretization equations, producing the finished GFM implementation. We consider a simple 1D case where the interface stands between cells C and E, while the gas phase is on the left and liquid phase is on the right of the interface as illustrated in Fig. 3.5. For this situation we need to modify the discretization of the pressure Laplacian for cells C and E, and the pressure gradient at the face e. The one-dimensional FV discretization of the pressure Laplacian and gradient terms (respectively in Eqs.3.49 and 3.50) for the cells C and face e appear as:

$$\nabla.\left[\frac{1}{A_P\rho}(\nabla P_d)\right] = \sum_{f\in\Omega_i}\left[\frac{1}{A_p\rho}\nabla P_d\right]_f .s_f = \left(\frac{P_{d_E}^g - P_{d_C}^g}{\delta x_e}\right)\frac{s_e}{\langle A_p\rangle_e \rho^g} - \left(\frac{P_{d_C}^g - P_{d_W}^g}{\delta x_w}\right)\frac{s_w}{\langle A_p\rangle_w \rho^g} \tag{3.51}$$

$$\frac{\nabla P_d}{A_P\rho}.s_f\,|_e = \left(\frac{P_{d_E}^g - P_{d_C}^g}{\delta x_e}\right)\frac{s_e}{\langle A_p\rangle_e \rho^g} \tag{3.52}$$

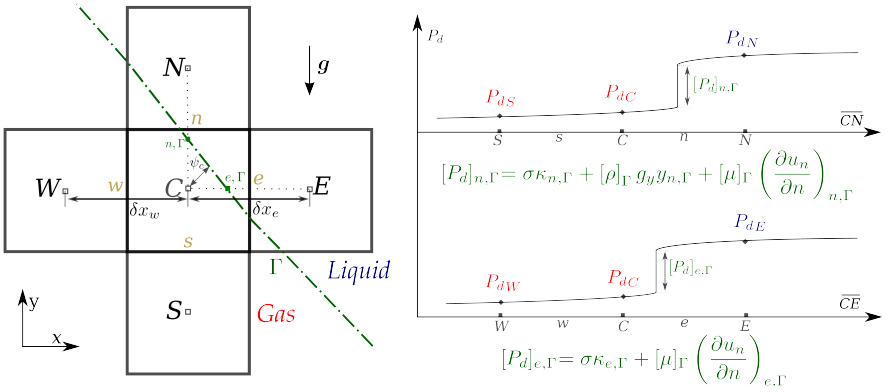

Figure 3.5: Schematic of 2D computational stencil where the interface locates between C and E, and C and N.

Since cell C is in the gas phase, a gas cell (ghost cell) is defined across the interface for cell E. The pressure jump relations between ghost and real cells at the interface may be created via Taylor series expansions about the interface. The relation at Ghost cell E is as follows:

$$[P_d]_E = [P_d]_\Gamma + (X_E - X_\Gamma)\left[\frac{\partial P_d}{\partial x}\right]_\Gamma + O\left((X_E - X_\Gamma)^2\right) \tag{3.53}$$

where $[P_d]_E = P^l_{d_E} - P^g_{d_E}$, and X denote coordinate vectors. Given the momentum equation (Eq.3.46), the assumption of a continuous velocity field across the interface leads to the condition of a continuous pressure gradient, $\left[\frac{1}{\rho}\nabla P_d\right]_\Gamma = 0$. By expanding and simplifying Eq.(3.54), we can evaluate the pressure gradient jump as:

$$\left[\frac{\partial P_d}{\partial x}\right]_\Gamma = -\rho^l\left[\frac{1}{\rho}\right]\frac{\partial P_d}{\partial x}\,|^g_\Gamma = -\rho^g\left[\frac{1}{\rho}\right]\frac{\partial P_d}{\partial x}\,|^l_\Gamma \tag{3.54}$$

Since cell C is in the gas phase, $\frac{\partial P_d}{\partial x}|_\Gamma^g$ from Eq. (3.55) is considered. The pressure gradient is evaluated at the cell phase as $\frac{\partial P_d}{\partial x}|_\Gamma^g = \frac{P_{d_E}^g - P_{d_C}^g}{\delta x_e}$. Given $[\frac{1}{\rho}] = \frac{\rho^g - \rho^l}{\rho^g \rho^l}$, substituting the pressure gradient term in the Taylor series (Eq. 3.54) and replacing the ghost variable as $P_{d_E}^g = P_{d_E}^g - [P_d]_E$ yields an expression for $[P_d]_E$:

$$[P_d]_E = [P_d]_\Gamma \frac{\rho^g}{\rho^\star} + \left(1 - \frac{\rho^g}{\rho^\star}\right)(P_E^l - P_c^g) \tag{3.55}$$

where the modified density is defined as $\rho^\star = \theta\rho_g + (1-\theta)\rho_l$ and the distance index, $\theta = \frac{|\psi_C|}{\delta x_e}$. The pressure jump relation at cell E for the ghost variable of pressure appears as:

$$P_{d_E}^g = P_{d_E}^l - [P_d]_E = -[P_d]_\Gamma \frac{\rho^g}{\rho^\star} + \left(1 - \frac{\rho^g}{\rho^\star}\right) P_{d_C}^g + \frac{\rho^g}{\rho^\star} P_{d_E}^l \tag{3.56}$$

By substituting the previous expression in the Laplacian discretization (Eq. 3.51), the final discretization becomes:

$$\nabla.\left(\frac{1}{A_p\rho}\nabla P_d\right)|_{@c} = \left(\frac{P_{d_E}^l - P_{d_C}^g}{\delta x_e}\right)\frac{s_e}{\langle A_p\rangle_e \rho^\star} - \left(\frac{P_{d_C}^g - P_{d_W}^g}{\delta x_w}\right)\frac{s_w}{\langle A_p\rangle_w \rho^g} - [P_d]_\Gamma \frac{s_e}{\langle A_p\rangle_e \rho^\star \delta x_e} \tag{3.57}$$

And the gradient term at face e (Eq. 3.52) is modified to be:

$$\frac{\nabla P_d}{A_p\rho}.s_f\,|_e = \left(\frac{P_{d_E}^l - P_{d_C}^g}{\delta x_e}\right)\frac{s_e}{\langle A_p\rangle_e \rho^\star} - [P_d]_\Gamma \frac{s_e}{\langle A_p\rangle_e \rho^\star \delta x_e} \tag{3.58}$$

The density at the cell face near the interface (face e) is replaced by the modified density $\rho^\star$. In the discretization of the viscous term (Eq. 3.46) the dynamic viscosity at the face needs to be replaced by the effective dynamic viscosity $\hat{\nu}$ [42, 47] in order to build the velocity coefficient matrix (Eq. 3.48). Therefore, the viscous term is shown:

$$\nabla.(\nu\nabla u_x)\,|_{@c} = \hat{\nu}\left(\frac{u_{xE} - u_{xC}}{\delta x_e}\right)s_e - \nu_e\left(\frac{u_{xC} - u_{xW}}{\delta x_w}\right)s_w \tag{3.59}$$

where the effective dynamic viscosity becomes:

$$\hat{\nu} = \frac{\nu^l \nu^g}{\Theta \nu^l + (1-\Theta)\nu^g} \tag{3.60}$$

The numerical solution procedure of decoupled pressure A-CLSVOF/GFM is illustrated in Fig.3.6.

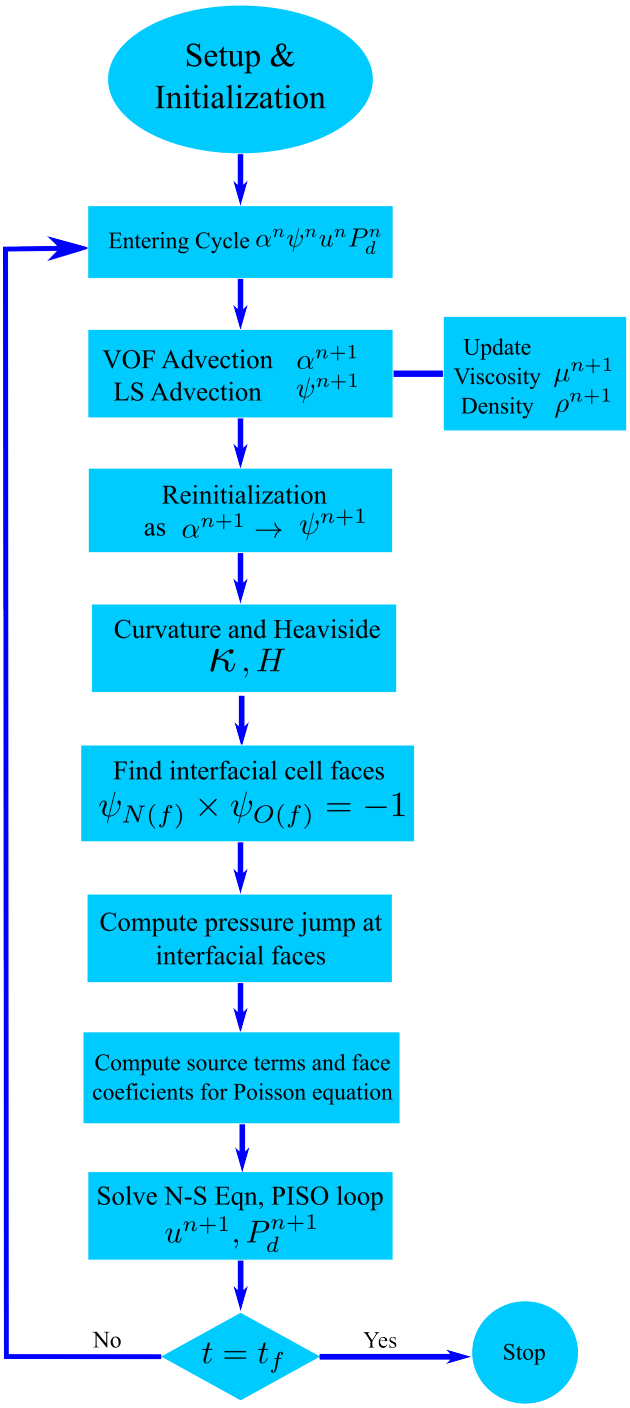

Figure 3.6: Flow diagram of A-CLSVOF/GFM method for one computational cycle.

3.4 Decoupled pressure CLSVOF/GFM

In this section, we present decoupled pressure PISO loop for implementation of interfacial forces such as surface tension, buoyancy and viscous force. While the governing equations are same as was driven in section 3.3.1. Here, the dynamic pressure P_d is separated into two pressure components:

$$P_d = P_1 + P_2. \tag{3.61}$$

Where P_1 accounts for interfacial forces while P_2 represents the rest of flow pressure. In this way, P_1 captures sharp transition at the interface, and P2 measures flow induced pressure without the effect of discontinuities at interface.

3.4.1 Decoupled pressure PISO loop

As was described, int the PISO solution velocity is predicted based old time n velocity and pressure. However here, the momentum predictor Eq.3.48 is computed based on P_1 as:

$$A_P u_P^\star + H(u_N) = -\frac{\nabla P_1^n}{\rho} \tag{3.62}$$

While P_1 needs to be computed prior to the execution of Eq.3.63. To compute P_1, Poisson equation $\nabla . \left(\frac{\nabla P_1}{\rho}\right) = 0$ is solved considering jump conditions which would appear as source terms on the

tight hand side. Therefore we have:

$$\nabla.\left[\frac{(\nabla P_1^\star)}{\rho}\right] = \nabla.\left(\frac{\left(\sigma\kappa - [\rho]g.x + [\mu]_\Gamma \frac{\partial u_n}{\partial n}\right) n\delta_\Gamma}{\rho}\right) \tag{3.63}$$

where P_1 follows jump condition:

$$[P_1]_\Gamma = \sigma\kappa - [\rho]_\Gamma g.x + [\mu]_\Gamma \frac{\partial u_n}{\partial n} \tag{3.64}$$

In worth mentioning that, the right hand side of Eq.3.64 is non-zero at interface and zero everywhere else. Given predicted velocity $u^\star$, PISO loop starts as:

$$u_P^{\star\star} = A_P^{-1}\left[H(u_N^\star) - \frac{\nabla P_2^\star}{\rho}\right] \tag{3.65}$$

The corrected dynamic pressure, $P_2^\star$, may be determined implicitly by imposing the continuity condition,

$$\nabla.\left[A_P^{-1}\frac{(\nabla P_2^\star)}{\rho}\right] = \nabla.[A_P^{-1}(H(u_N^\star)] \tag{3.66}$$

Then the corrected velocity, $u_P^{\star\star}$ may be determined according to Eq.3.66. Accordingly, face fluxes of velocity are constructed at each face:

$$\phi^{n+1} = A_P^{-1}[H(u_N^\star)].s_f - A_P^{-1}\frac{\nabla P_2^\star}{\rho}.s_f \tag{3.67}$$

This process may be repeated from Eq.3.66 until sufficient convergence is met. The numerical solution procedure of decoupled pressure A-CLSVOF/GFM is illustrated in Fig.3.7.

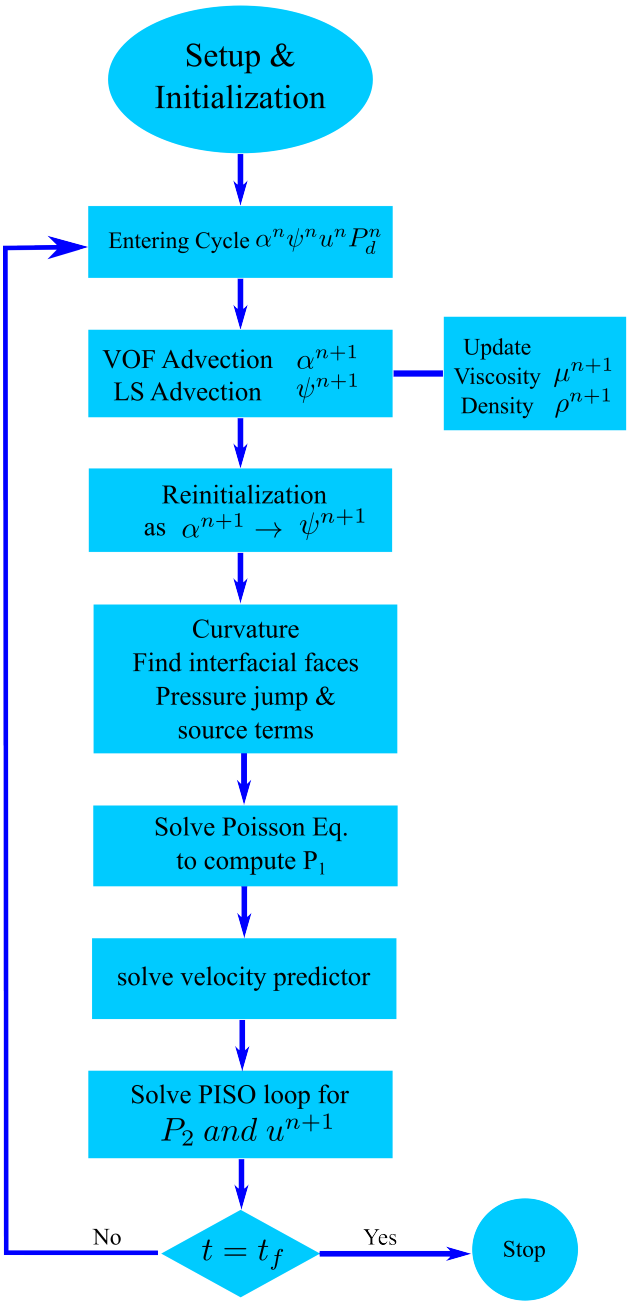

Figure 3.7: Flow diagram of decoupled pressure A-CLSVOF/GFM method for one computational cycle.

3.5 Turbulence modeling

In order to incorporate turbulent instabilities for the oil spill cases with high Reynolds numbers, large eddy simulation (LES) turbulent modeling is applied. Different LES models are available in the OpenFoam framework. In this research, we used a one equation model for finding subgrid scale (SGS) kinetic energy and smooth filtering coefficient. By means of eddy viscosity and SGS kinematic viscosity, the SGS stress tensor is approximated as follows [**?**]:

$$\tau_{SGS} = \overline{vv} - \bar{v}\bar{v} \tag{3.68}$$

$$\tau_{SGS} - \frac{2}{3}k_{SGS}I = -\frac{\mu_{SGS}}{\rho}[\nabla\bar{v} + (\nabla\bar{v})^T] \tag{3.69}$$

$$\frac{\partial k_{SGS}}{\partial t} + \nabla.(k_{SGS}\bar{v}) = \nabla.[(\vartheta + \vartheta_{SGS})\nabla k_{SGS}] - \varepsilon - \vartheta_{SGS}\bar{S}^2 \tag{3.70}$$

In which, ε, ϑ_{SGS} and $S^{'}$ are calculated according to following relations:

$$\varepsilon = \Delta C_\varepsilon (k_{SGS})^{\frac{3}{2}}, \quad C_\varepsilon = 1.05 \tag{3.71}$$

$$\vartheta_{SGS} = \Delta C_k (k_{SGS})^{\frac{1}{2}}, \quad C_\varepsilon = 0.07 \tag{3.72}$$

$$\bar{S} = \frac{1}{2}[\nabla\bar{v} + (\nabla\bar{v})^T] \tag{3.73}$$

CHAPTER 4
RESULTS

This chapter presents our numerical results including evaluation test cases for A-CLSVOF/CSF, ghost fluid method (A-CLSVOF/GFM) and decoupled pressure method (DPM) solvers, and also numerical study on oil jet in cross-flow water. In order to evaluate the A-CLSVOF method, we utilized four canonical two-phase flow cases where the capillary force is either prevails or is on the same order as other forces (viscous, inertial and buoyant) either during the entire simulation, or during some critical, definitive period. For these studies, the interaction of capillary forces with 1. the onset of spurious currents 2. viscous dissipation 3. gravity and 4. inertial forces are considered, covering a spectrum of scenarios common to many physical problems in multiphase flows.

To evaluate the A-CLSVOF/GFM method, we utilized four canonical two-phase flow cases. For the static droplet, the interaction of the capillary force with the spurious currents and viscous dissipation are considered, which demonstrates the ability of the GFM to reduce the presence of spurious currents. The case of capillary wave relaxation shows the accuracy of surface tension implementation. For the case of linear shear flow, GFM implementation of the viscous term is compared with the CSF method. The rising bubble case incorporates all proposed modifications and compares the present implementation with CSF and published experimental results.

The decoupled pressure method (DPM) is assessed by simulation of static droplet and capillary wave relaxation cases. For static droplet case, the accuracy of method in pressure prediction and generation of spurious currents are studied. Simulation of capillary wave relaxation reveals the efficiency of new implementation compared to the base PISO loop.

Oil jet behaviour in quiescent and cross-flow water is studied. Four jet breakup modes including dripping, axisymmetric jetting, asymmetric jetting and atomization are reported for different combination of non-dimentional numbers. Effect of flow and fluid properties on jet breakup pattern are analysed and regime maps are reported.

4.1 A-CLSVOF method

The first simulation benchmarks A-CLSVOF against VOF and its predecessor, CLSVOF for a 2D droplet in equilibrium, or a static droplet. For both coarse and fine grids, the pressure distribution along the internal and external region of the droplet will be considered along with the quantification of maximum and average transient velocity values resulting from the onset of parasitic currents.. Next we consider the oscillating relaxation of an initially perturbed fluid interface and compare our result with the theoretical solution. The error of the A-CLSVOF method are compared to the results reported in other studies. Third, we consider a non-linear Rayleigh-Taylor instability where inviscid, buoyant forces propel feed the growth of an interface. Our result is qualitatively compared with work reported in another study. Finally, a droplets impact on liquid pool was considered in order to assess the combination of all of the aforementioned physical processes as well as inertia.

Grid independence illustrates the present models ability to resolve sub-grid interfacial curvature and final results are compared to the VOF method and finally, to experimental results present in another study.

4.1.1 Equilibrium droplet

The first case study assess our methods ability to accurately resolve the interfacial curvature and ultimately reduce the presence of parasitic currents. It is a well-known and greatly studied consequence that the implementation of the CSF can result in spurious currents or non-physical velocities that are propelled and fed by the capillary flux at the interface. These fluxes, depending on their relative magnitude, will skew any other physical process that involves convection (enthalpy, species concentration during interfacial mass transfer etc.) as these quantities will be swept away and mixed with regions away from the interface, artificially increasing the perceived rate of diffusion or migration to or from the interface. Not only will the results be inaccurate, but the time step restrictions due to stability can be many orders of magnitude higher than the restrictions on the time scale typically required for resolving slow processes such as mass diffusion across liquid/vapor interfaces. The adverse effects of these currents become more pronounced in in situations involving high density ratios of fluid phases, high surface tension coefficient and low internal and free stream velocities relative to the magnitude of the currents that would be generated in a static case. For the test presented here, in the absence of any external force such as gravity, the surface tension

force that maintains the droplet symmetry produces a pressure difference across the interface and is known as the Young-Laplace pressure.

The mesh domain measures $0.1m \times 0.1m$ and is comprised of uniformly distributed cells measuring $\Delta x = 2mm$ and $\Delta x = 1mm$ for the coarse and fine grids where the drop is initialized with a radius of $R_d = 0.02m$. The simulation time step is set to $\Delta t = 0.1\Delta x$. The physical properties for the droplet (liquid phase) are $\rho_l = 1000kg/m^3$, $\mu_l = 0.001kg/ms$, and for surrounding (gas phase) are $\rho_g = 1kg/m^3$, $\mu_l = 10^{-5}kg/ms$, while the surface tension is $\sigma = 0.05kg/s^2$. The numerical pressure difference is compared to the 2D Young-Laplace equation as:

$$P_{exact} = \sigma k = \frac{\sigma}{R_d} \tag{4.1}$$

In which R_d is droplet radius. The analytical pressure jump condition for the droplet is $P_{exact} = 2.5Pa$. In order to compare our results with the exact value, the droplet pressure P_d in the simulation is calculated as:

$$P_d = \frac{1}{N_d} \sum_{i=1}^{N_d} P_i \tag{4.2}$$

where the sum averages over N_d liquid cells ($\alpha > 0.5$), the uniform pressure inside the droplet. Also, in order to study pressure error, two error norms of L_1 and L_2 are defined as follows:

$$L_1 = \left| \frac{\sum_{i=1}^{N_d} (P_i - P_{exact})}{N_d P_{exact}} \right| \tag{4.3}$$

$$L_2 = \left| \frac{\sum_{i=1}^{N_d} (P_i - P_{exact})^2}{N_d P_{exact}^2} \right|^{\frac{1}{2}} \tag{4.4}$$

In the Table 4.1, the maximum and average velocity (U_{max}, U_{ave}) are reported to analyze the spurious currents at the pseudo-steady state time selected to be $1s$. The ratio of the numerical pressure

to the analytical value (P_d/P_{exact}) and pressure error norms (L_1, L_2) for both coarse and fine grids are also presented in Table 4.1. For the coarse grid, S-CLSVOF showed higher spurious currents than VOF, which is consistent with the findings reported by Albadawi et al. [61]; A-CLSVOF decreased these nonphysical currents even for the coarse grid. Comparison of the pressure ratio and the error norms indicate that A-CLSVOF is in good agreement with the analytical pressure even for coarse grid, while VOF and SCLSVOF show about 20% and 10% error (L_1 norm). For the fine grid, S-CLSVOF demonstrated and improvement relative to VOF, however both methods showed drastically higher parasitic currents compared to A-CLSVOF. The pressure calculation illustrates that even for a relatively coarse grid, A-CLSVOF produced a pressure consistent with the Young-Laplace prediction while the other methods demonstrate some considerable discrepancy.

Table 4.1: Study of spurious currents and pressure error between three methods.

Methods	Grid Size [mm]	$U_{max}[m/s]$	$U_{ave}[m/s]$	P_d/P_{exact}	L_1	L_2
VOF	2	0.0038	0.004	0.848	0.2	0.24
	1	0.00056	0.0005	0.884	0.13	0.16
S-CLSVOF	2	0.109	0.02	0.942	0.1	0.17
	1	0.0036	0.00016	0.967	0.51	0.112
A-CLSVOF	2	0.00025	$4.2e-5$	0.992	0.038	0.11
	1	$7.8e{-}5$	$1.1e-5$	0.999	0.016	0.077

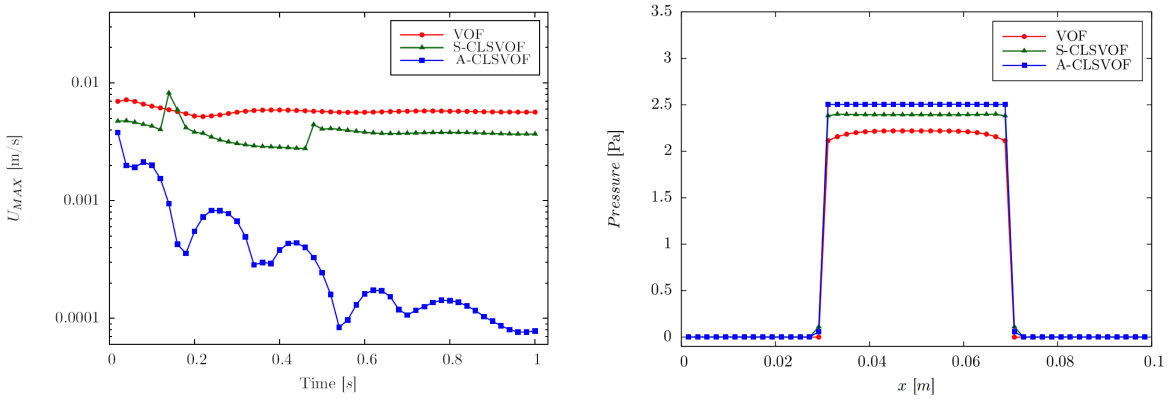

Figure 4.1: (a) Plot of U_{max} as a function of time, (b) comparison of pressure distributions at centerline and, for fine grid of $\Delta x = 1mm$.

The maximum velocity in the domain resulting from parasitic currents is shown over a simulation time of $1s$ in Fig.4.1(a). The result demonstrates that A-CLSVOF quickly diminished the parasitic currents compared to VOF and S-CLSVOF methods. It is important to note that there is an initial relaxation of the interface as the initial numerical setup of the volume fraction produces a non-physical interface distribution that the surface tension forces work to redistribute. Pressure distribution across the center of the droplet is shown in Fig.4.1(b), and illustrates how our method accurately captures the sub-grid scale curvature of a circular interface, even on a uniform hexahedral grid. The inability of the other methods to capture such a precise estimation of the interface orientation manifests itself in the resulting pressure distribution.

4.1.2 Capillary wave relaxation

This case examines the interaction of capillary and viscous forces in the absence of gravity. An initially perturbed and stationary wave is allowed to oscillate where shear stresses serve as the mechanism for energy dissipation [62]. Prosperetti [63] reported an initial-value solution for the wave amplitude versus time and is utilized here to calculate the error. The parameters and computational domain are set to be consistent with [62]. The domain width is consistent with wavelength $H = \lambda = 2\pi/K$ where the two fluids have equal density and kinematic viscosity $\rho_l = \rho_g = 18.3kg/m^3$ and $\nu_l = \nu_g = 0.0043m^2/s$ which result in non-dimensional viscosity of $\varepsilon = \mu K^2/\rho\omega_o = 0.06472$. Here, K is wave number and ω_o is given as $\sigma K^3/(\rho_l + \rho_g)$. For this, the study Ohnesorg number is set as $Oh = \mu/(\sigma\rho_l\lambda)^{0.5} = 1/\sqrt{3000}$. The error for the simulation is calculated as:

$$E_2 = \frac{1}{\lambda}\sqrt{\frac{\omega_0}{25}\int_{t=0}^{\frac{25}{\omega_0}}(h - h_{exact})^2} \tag{4.5}$$

where h is measured from a fixed point where the wave has no amplitude. Two uniformly distributed grids are considered in this study taking 32^2 and 64^2 cells respectively. The capillary amplitude is plotted versus time in Fig.4.2 for the current model as well as VOF and the theoretical solution for the same grid configuration of 642 cells.

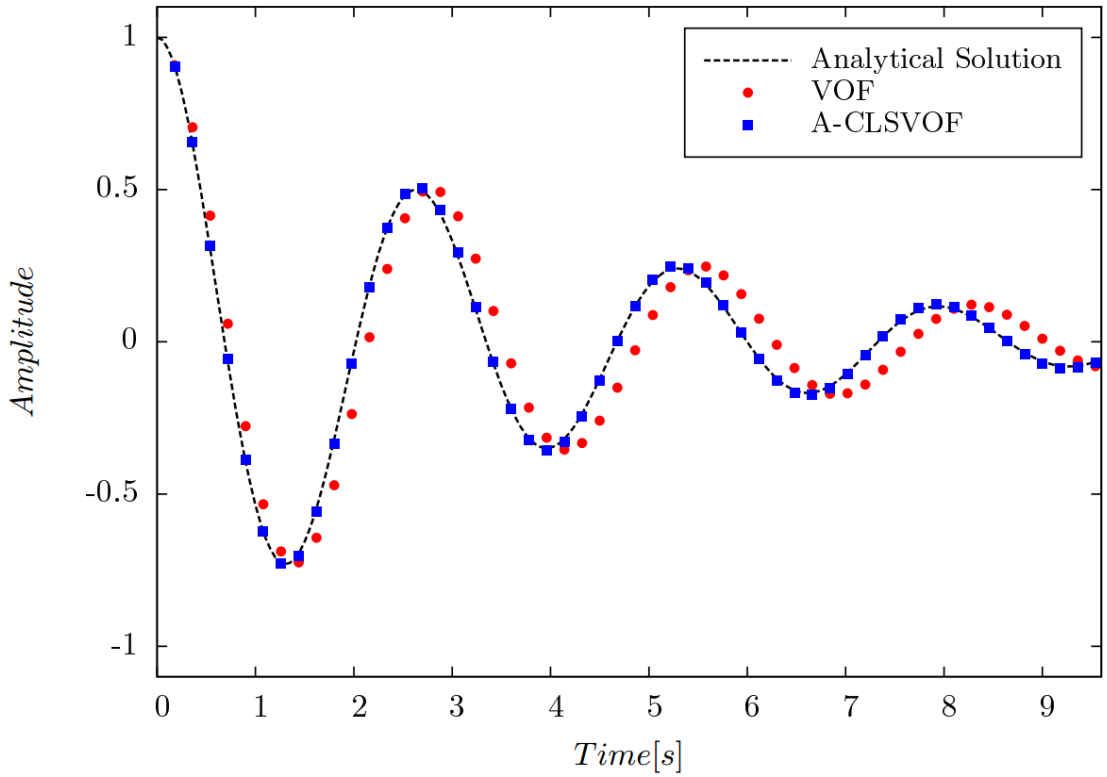

Figure 4.2: Time evolution of capillary wave amplitude compared with analytical solution for grid 64^2.

The A-CLSVOF method indicated excellent agreement with the theoretical solution, while the VOF method exemplifies considerable error. Table 4.2 presents the error calculations of four methods including results for CLSVOF and Front tracking methods presented in other studies for an identical configuration [64, 62].

Table 4.2: Relative error E_2 for capillary wave time evolution for different methods.

Grid/Method	VOF	A-CLSVOF	CLSVOF [64]	Front Tracking [62]
32^2	0.51	0.032	0.0131	0.0131
64^2	0.0453	0.00609	0.0033	0.0098

According to the results, A-CLSVOF demonstrates comparable error when compared to CLSVOF and especially the Front tracking method. Table 4.2 indicates IS-CLVOF outperforms VOF for both grid numbers as well as Front tracking with moderate grid refinement. An important note here is that for the refined grid, one that would typically be found in most practical applications, A-CLSVOF is on the same order $(< 1\%)$ as the more complex and computationally expensive CLSVOF method, making the use of the current model more attractive from a cost-accuracy stand point.

4.1.3 Rayleigh-Taylor instability and level set advection

The Rayleigh-Taylor (RT) instability of two different fluids layers occurs when the heavier fluid sits on top of the lighter fluid. Gravity drives the initialized interfacial perturbation into the less dense fluid, resulting in a plume like formation. . In this section, we consider the RT instability in order to assess our methods capabilities in handling capillary-buoyant force competition to qualitatively compare our result with the result reported by Zuzio and Estivalezes [65] who uti-

lize an adaptive mesh refinement Level Set method with a ghost fluid model. Other studies have reported qualitatively similar result [62, 66]. The simulation here is also utilized to illustrate the improvements in both computational cost and accuracy through the use of Level-Set advection.

The case parameters here are consistent with [65] with a rectangular domain of width $W = 1m$ and height $H = 4m$. The domain is comprised of a uniform mesh $\Delta x = 7.8mm$ ($N_x = 128, N_y = 512$). The side boundaries of the domain are modeled with slip conditions since the formation of these plumes would repeat periodically in either direction. The density of the heavier and lighter fluids are $\rho_h = 1.225kg/m^3$ and $\rho_l = 0.1694kg/m^3$ respectively, while both have equal viscosity, $\mu = 3.13 \times 10^{-3} kg/m.s$. The surface tension coefficient is set to $\sigma = 0.001337N/m$ and the interface is initialized as a sinusoidal perturbation about the elevation $y = H/2$ with an amplitude of $A = 0.05m$, a period of L and where $K = 2\pi/L$.

$$y_0 = \frac{H}{2} - Acos\left(K(x - \frac{L}{2})\right) \tag{4.6}$$

To analyze RT instability results, the interface topography is presented at six different solution time in Fig.4.3 in accordance with results reported by Zuzio and Estivalezes [65] who utilized the aforementioned model features. Our methods results compared well with the cited findings reprinted here but also with those found in other studies [62, 66].

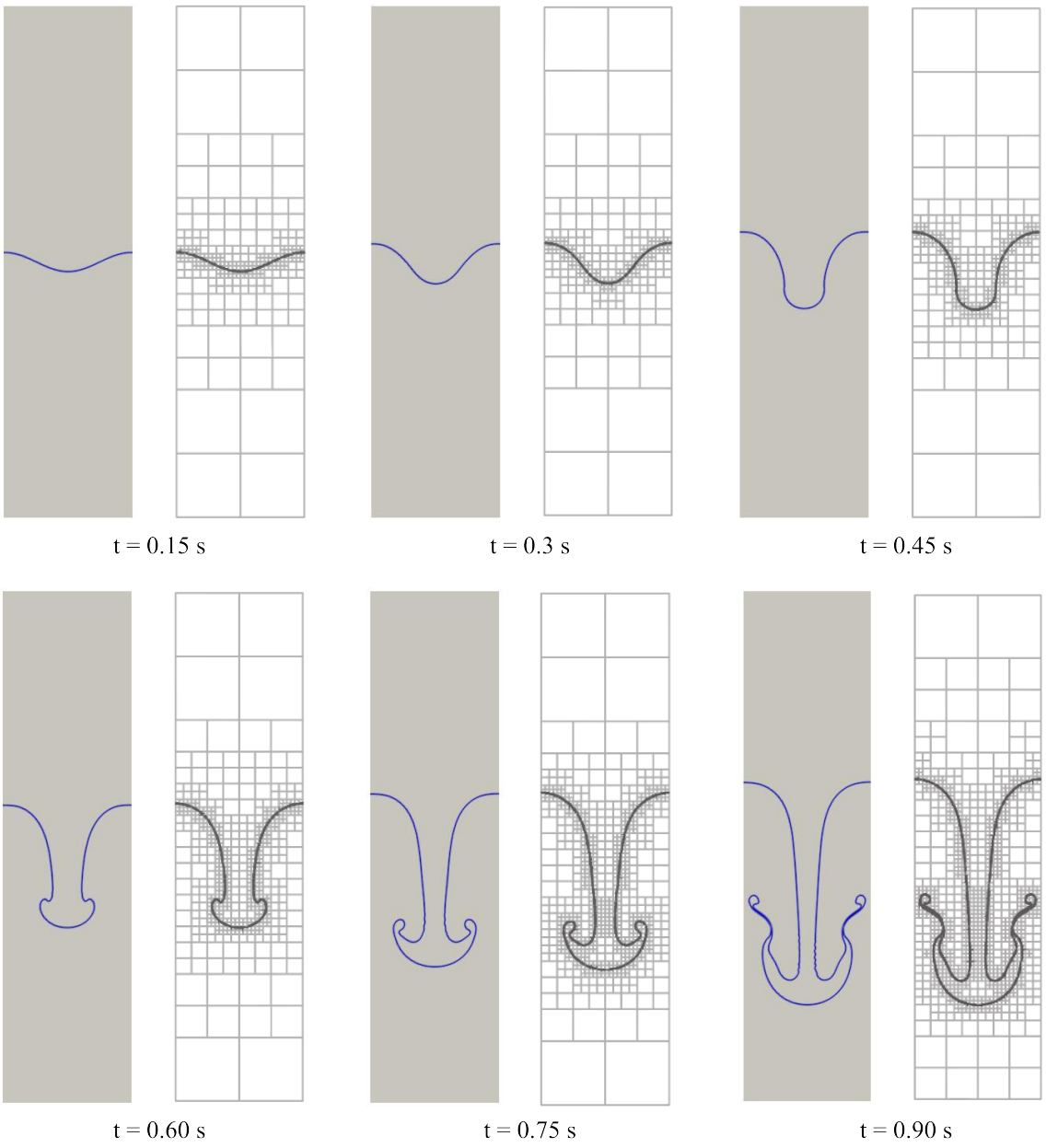

Figure 4.3: Comparison of Rayleigh-Taylor instability evolution, (solid background) current A-CLSVOF model and (representation with local gridrefinement) Zuzio and Estivalezes.

Furthermore, a 3D RT instability is simulated using the same properties as the 2D case. For this study, the simulation domain is discretized with a cell network of $128 \times 128 \times 512$ consistent with the 2D grid size. Fig.4.4 illustrates the time evolution of the 3D RT instability in a periodic domain. The interface location along the boundaries demonstrates physical similarities when compared to the 2D simulations as these periodic faces result in a no-flow/slip style condition. It is evident that the core of the dense fluid in the 3D case penetrates at a faster rate when compared to the 2D case. This is a result of the ability of the less dense fluid to be displaced in three dimensions around the advancing interface where the 2D fluid displacement is constrained in plane, resulting in greater flow resistance and ultimately, a slower penetration rate.

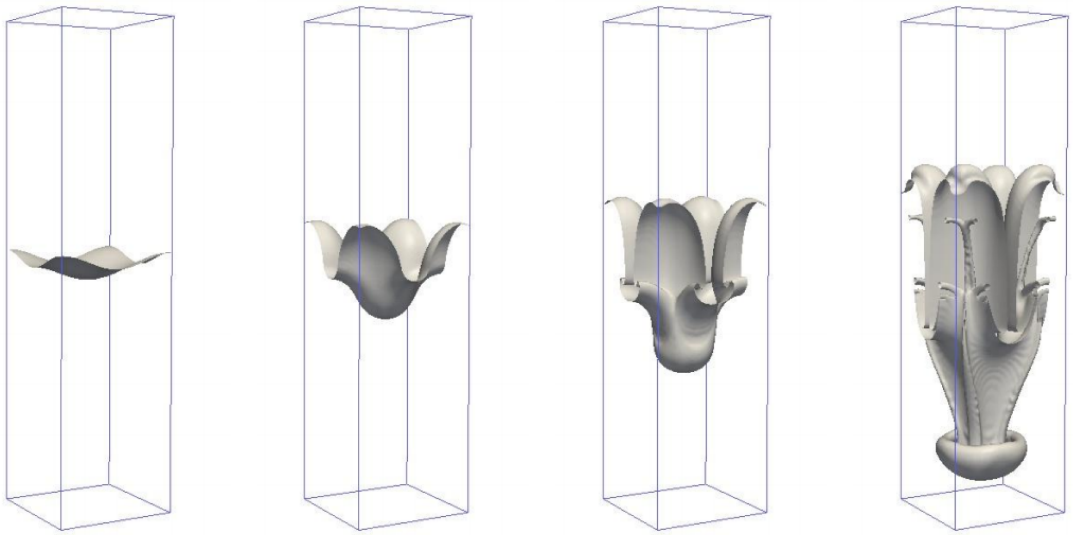

Figure 4.4: Time evolution of 3D Rayleigh-Taylor instability simulation.

As described in the numerical formulation section, the LS function ψ is advected to expedite the simulation by providing an initial guess for the to-be-reinitialized distance field, ψ_0. In order to illustrate the effect of LS advection on computational cost, the number of reinitialization iterations over the artificial time required to reach a steady state solution is plotted versus time (left y-axis Fig.4.5) for two simulations, one without LS advection and the other with LS advection. The steady state reinitialization error, $\varepsilon_{|\nabla\psi|} = \iiint(|\nabla\psi| - 1)dV / \iint dV$, is plotted (right y-axis Fig.4.5) to verify the error remains minimized, even while using advection.

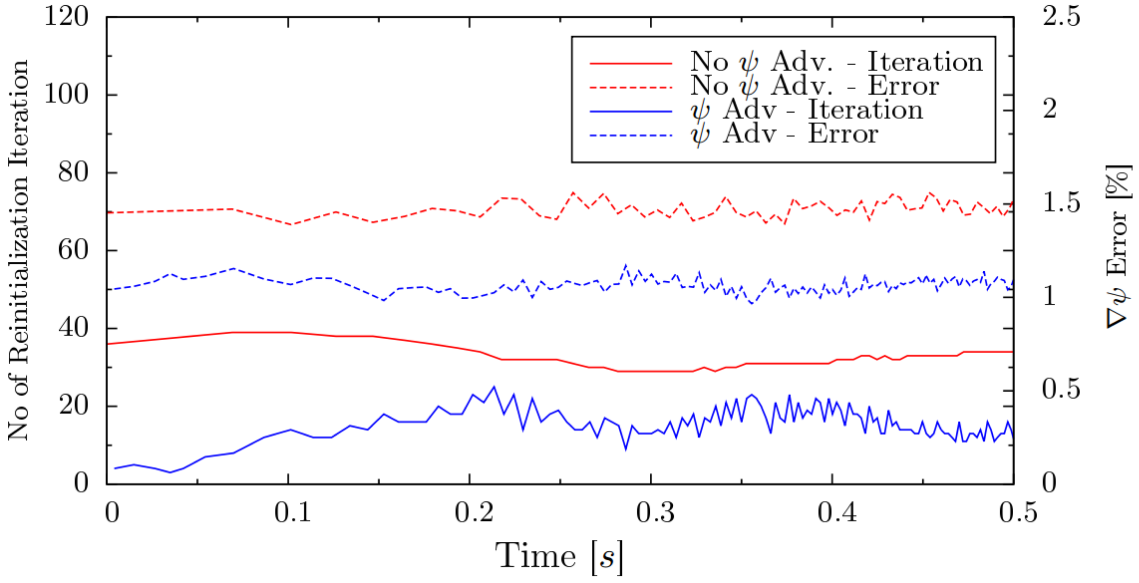

Figure 4.5: Number of reinitialization solution and LS field error versus time.

The final results for this case of study demonstrate two key features associated with the addition of LS advection: 1. the reduction in iterations over the artificial time step required to reach steady state and 2. a reduction in $\varepsilon_{|\nabla\psi|}$ when the final steady state result was reached. Since the seed points at the interface for ψ_0 are still computed from the mass conservative VOF field, the advection of

ψ does not result in any additional accumulation mass loss, common in early LS methods, when compared to the non advected case. In fact, fewer iterations and increased relaxation at the interface added by Eq.3.23 since $|\nabla\psi^{\tau=0}| \sim 1$ act to minimize both the incremental rate of migration and the total migration of the zero-level-set, implying that our advected and redistanced ψ not only improves the smoothness of the converged result through reduction in $\varepsilon_{|\nabla\psi|}$, but coherence with the mass conservative volume fraction. It has now been demonstrated that the proper conditioning of ψ_0 can serve as a crucial tool for the improvement of efficiency and accuracy of reinitialization methods, especially when temporal schemes call for an additional time step solution to advance one step in artificial time as was the case in this study and is shown in Eq.3.22. The addition of LS advection resulted in a $\sim 45\%$ reduction computational time for this case study.

4.1.4 Droplet impact

The final case considered incorporates high inertial and capillary forces and buoyant forces resulting from a large density ratio. The impact of liquid droplets of various compositions on pools has gone through exhaustive research covering a range of scenarios due to its relevance in applications including spray cooling, drop manipulation, forensic bloodstain analysis etc. [67]. The authors of this study recently conducted an experimental/numerical investigation of drop impact on a liquid pool resulting in Rayleigh jet formations and the generation of secondary droplets. In this section, the A-CLSVOF method is used to simulate these physics where the results will be compared to our previously published experimental and numerical VOF results.

In this study, the droplet and the pool are both of the same liquid (Silicone oil $5cSt$), while the continuous phase is air. The droplet of $d_p = 1.8mm$ collides with the free surface of a $13mm$ deep pool with an impact velocity of $1.8m/s$ ($Oh = 0.0360$). Silicone oil has a density of $\rho = 0.91g/cm^3$, viscosity of $\mu = 5cSt$ and an interfacial surface tension coefficient with air of $\sigma = 19.7mN/m$. Since the droplet impact behaves in an axisymmetric manner, our simulation exploits this to our benefit for both computational efficiency and to demonstrate another functional configuration for the A-CLSVOF method.

The computational domain utilizes local grid refinement in the anticipated splash region and a coarser grid in regions where pressures and velocities are relatively low. $50\mu m$, $25\mu m$ and $15\mu m$ grid spacing were tested in the splash region with a constant, coarse grid in the free stream, consistent with published VOF simulation. The interface height is measured relative to the initial free surface elevation and tracks the motion of the free surface along the axis sharing the impact trajectory. As the interface recoils, forming a Rayleigh-jet, pinch-off occurs and the interface being tracked switches from the top of the jet/droplet back to the free surface of the pool. The free surface interface height is presented in Fig.4.6(a) from the moment of impact till the onset of the first oscillation of the free surface following the pinch-off of the daughter drop for the three grids considered. The height variation includes three distinct regions consisting of regions: A. crater formation after initial impact, B. Rayleigh-jet formation by capillary force and C. secondary droplet pinch-off. Our method achieved grid independence for a $25\mu m$ grid size, where the VOF method required a $10\mu m$ spacing to achieve a grid independent solution.

It is evident from Fig.4.6(b) that A-CLSVOF out performs the VOF method in regions B and C where capillary forces play a greater role in the resulting trajectory of the interface height. The error of maximum height and size of secondary droplet were 0.4% and 1.4%, respectively and were measured by integrating the volume of the phase fraction after detachment. The simulation results interface contours are qualitatively compared with the experimental result in Fig.4.7 at ten different solution times. According to the qualitative comparison, our simulation qualitatively agrees with the experimental images.

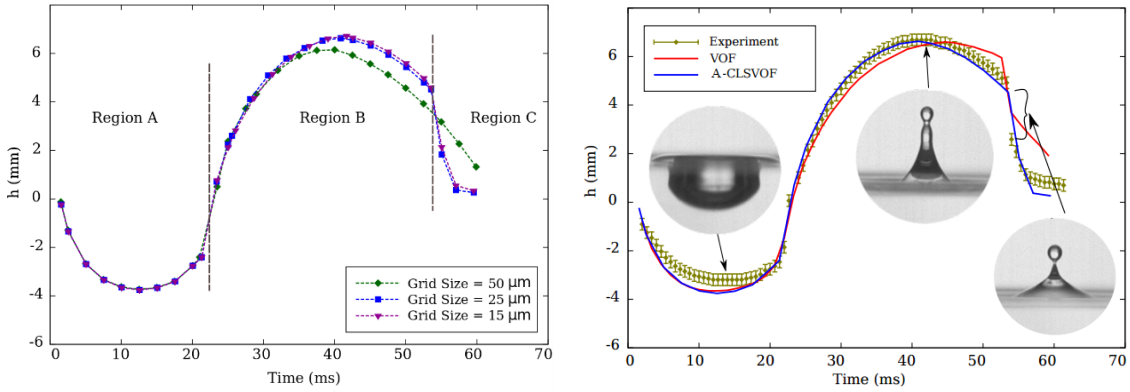

(a) (b)

Figure 4.6: Grid independence study on interface height variation. b) Comparison of our numerical interface time evolution with experiments.

Some important attributes of the proposed model can be inferred from this last simulation. As the former simulations have suggested, A-CLSVOF predicts sub-grid curvature extraordinarily well when compared to S-CLSVOF and especially VOF. The results produced by VOF did not show gradual convergence as the grid was refined; instead, the results were erratic in the transition between grids and in regions B and C identified in Fig.4.6(b) while even for the finest grid, still

failed to produce a result that was consistent with the experimental findings. It becomes evident that the VOF method, even for excessively fine grids, fails to model sub-grid interface orientation is estimated from bulk volume fractions of neighboring cells on grids where cell size and orientation can greatly influence local curvature calculations. As a corollary to the previous finding, the use of the LS function and the filtering described in this study for the current A-CLSVOF model allows for an accurate estimation of the sub-grid scale interface curvature. The deficiencies outlined in this study for VOF and S-CLSVOF method draw attention to the fundamental need for the proposed A-CLSVOF model, not only for the requirement to accurately model capillary forces, but for the ability to quickly and efficiently handle topological changes, even on relatively coarse grids, a feature that VOF and S-CLSVOF simply cannot offer.

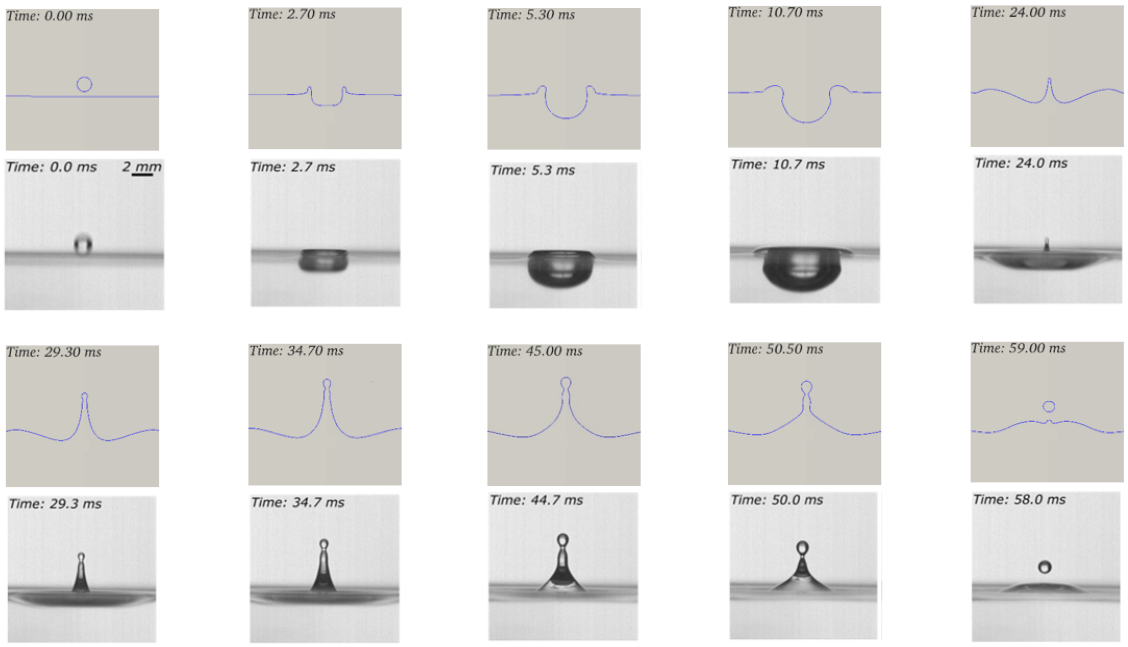

Figure 4.7: Qualitative comparison of our numerical result and experimental result of interface evolution.

4.2 A-CLSVOF/Ghost fluid method

In this section we utilize four two-phase flow cases to assess the GFM implementation on A-CLSVOF solver. 1) Static droplet case, which shows capabilities of our methods to predict pressure and diminish spurious currents. 2) Capillary wave relaxation, that shows the accuracy of surface tension implementation using GFM. 3) Linear shear flow case, shows effect of CSF implementation on dissipation of shear forces versus the GFM implementation. 4) Rising bubble case, for which

we use the solver incorporating GFM implementation of all interfacial forces and compare with CSF implementation and also a published experimental results.

4.2.1 Static droplet

The first case study assesses the ability of the present implementation of GFM to resolve the surface tension force and ultimately reduce the presence of spurious currents. It is a well understood that the implementation of CSF can result in spurious currents or non-physical velocities that are propelled and fed by the capillary flux at the interface region. The mesh domain measures $1m \times 1m$ and is comprised of uniformly distributed cells measuring $\Delta x = 0.01m$, where the drop is initialized with a radius of $R_d = 0.25m$. The simulation time step is set to $\Delta t = 0.1\Delta x$. The physical properties for the droplet (liquid phase) are $\rho_l = 10$ and $1000kg/m^3$, $\mu_l = 0.001kg/ms$, and for the surrounding gas phase are $\rho_g = 1kg/m^3$, $\mu_g = 10^{-5}kg/ms$, with $\sigma = 0.05kg/s^2$. The numerical pressure solution can be compared with the analytical value by the 2D Young-Laplace equation as Eq.4.1.

Table 4.3: Parasitic currents and pressure comparison (at 50 time steps) between CSF and GFM.

Method	$\frac{\rho_l}{\rho_g}$	U_{max}	U_{ave}	L_1	L_2
A-CLSVOF/CSF	10	0.041	$5.9e-4$	0.025	0.097
	1000	0.042	$3.1e-4$	0.021	0.129
A-CLSVOF/GFM	10	0.012	$2.1e-5$	$6.7e-4$	0.006
	1000	$2.4e-4$	$5.7e-6$	0.004	0.022

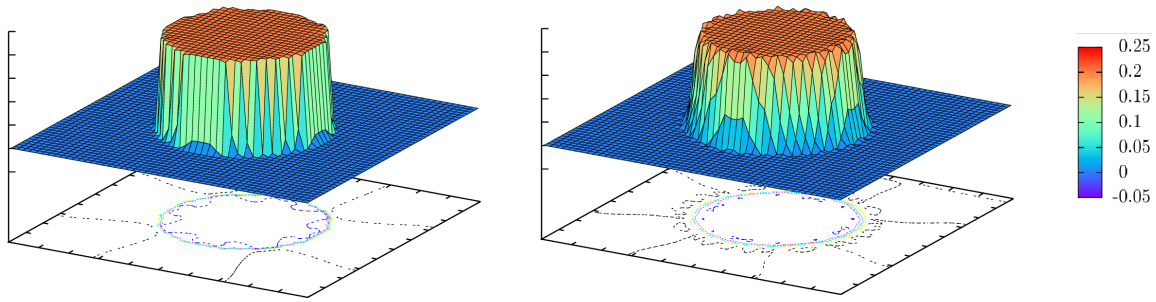

(a) (b)

Figure 4.8: Pressure distribution of a static 2D drop after 10 time steps. Density ratio is $\rho_l/\rho_g = 10$, a) GFM and b) CSF.

In Table 4.3, the maximum and average velocity (U_{max}, U_{ave}) are reported to analyze the spurious currents at 50 time steps. The pressure error norms (L_1, L_2) for both density ratios of 10 and 1000 are also presented. Comparison of GFM and CSF methods shows that the explicit implementation of the capillary pressure jump decreased the non-physical currents substantially. For the high-density ratio, our solution dropped the spurious currents two orders of magnitude. Com-

parison of the pressure error norms indicates that GFM is in good agreement with the analytical pressure, even for high density ratios, while CSF demonstrate some considerable discrepancy. The improvements in the numerical model of the GFM over the CSF method for treating the capillary force is evident. In Fig. 4.8, pressure distributions obtained from the CSF and GFM are compared, with interfaces tracked by the A-CLSVOF method. As anticipated, a sharp pressure profile is created by the GFM, while the pressure jump is smeared across several cells in the CSF scheme.

4.2.2 Capillary wave relaxation

Capillary wave relaxation shows the interaction of capillary and viscous forces in the absence of gravity of an initially perturbed interface. The present method is tested using the same properties as 4.1.2 and is compared to the analytical solution for the wave amplitude versus time for two grid resolutions. The capillary amplitude is plotted versus time in Fig.4.9 for coarse and fine grids. The A-CLSVOF/GFM method is in good agreement with the analytical solution and demonstrates the accuracy in the capillary and viscous forces at the interface when compared to the theoretical solution.

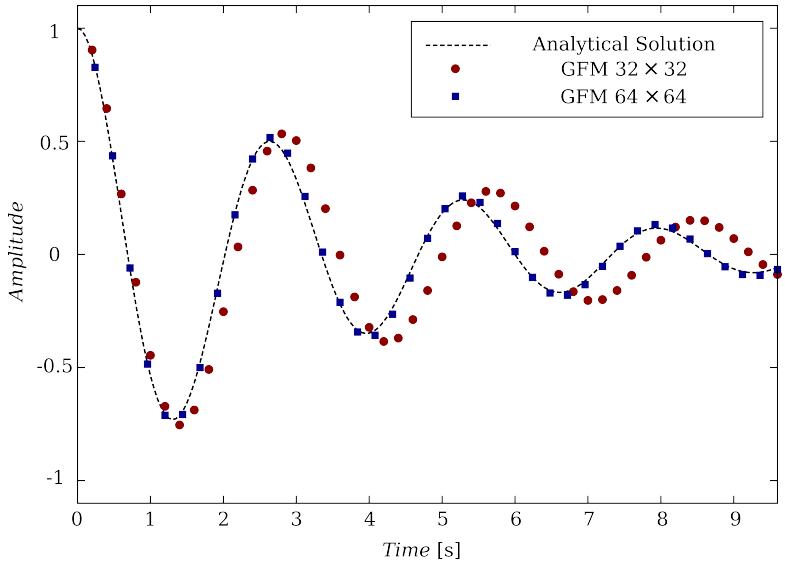

Figure 4.9: Capillary wave oscillation versus time. The GFM result is compared with the analytical solution.

4.2.3 Linear two-layer shear flow

Linear two-layer shear flow between two parallel walls is considered to examine the tangential shear stress evaluated using CSF and GFM implementation of normal components of the viscous term. A square domain is considered where the left and right boundaries are periodic, and the top and bottom walls are moving at 1 and $-1m/s$ respectively (Fig.4.10). The computational domain is discretized by 40 cells in each direction. Simulation properties are as follows: $\rho_l = \rho_g = 1kg/m^3$, $\mu_l = 0.1Pa.s$ and $\mu_g = 0.005Pa.s$. The horizontal velocity profile at steady state is plotted against the analytical solution in Fig.4.10. The improvements in accuracy added by GFM sharp treatment

of the viscosity across the interface can be seen as a sharp gradient of the horizontal velocity in the vertical direction. The otherwise diffusive averaging of the viscosity used in CSF results in an over prediction in the tangential stress in the upper gaseous phase associated diffusive discretization across the interface.

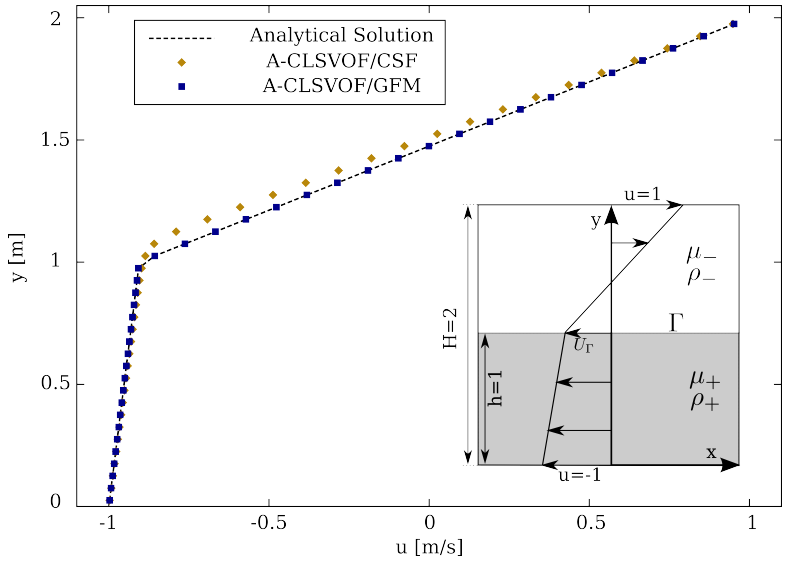

Figure 4.10: Steady state horizontal velocity profile predicted by CSF and GFM treatment of viscous term.

4.2.4 Deformed rising bubble

In order to complete the assessment of our GFM implementation, the buoyancy term is tested by the rise of a spherical cap bubble in a highly viscous liquid and compared to an experimental study [68]. For this case, an axisymmetric computational domain is defined as $l_r = 4D_b$ (D_b is the initial bubble diameter) and $l_z = 4l_r$, which is discretized by grid 128×512. The following properties are

considered for the simulation: $\rho_l = 875.5kg/m^3$, $\rho_g = 1kg/m^3$, $\mu_l = 0.118Pa.s$, $\mu_g = 0.001Pa.s$, $D_b = 0.0122m$, $\sigma = 0.033N/m$. In Fig.4.11, the bubble velocity is plotted at various times to establish the final terminal velocity where gravitational forces balance viscous stresses. In this case, all mechanisms of the present GFM are tested as the steady bubble profile is dictated by the balance of gravitational, viscous and capillary forces at the interface. The simulation results for GFM and CSF are compared to the reported experimental result for terminal velocity, $U_t = 21.5cm/s$. As shown, the terminal velocity of the GFM is in good agreement with the experimental result, while the CSF shows relatively considerable error, 4.6% and 14% respectively.

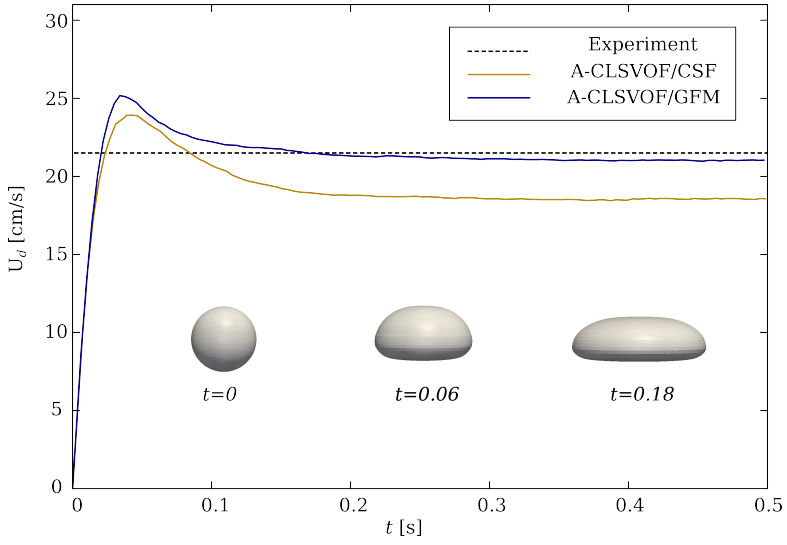

Figure 4.11: Temporal evolution of the droplet velocity U_d for different singular term implementation. The present simulation result is compared with experimental terminal velocity.

4.3 Decoupled pressure A-CLSVOF/GFM method

In this section, we evaluate the decoupled pressure method (DPM)implementation of A-CLSVOF/GFM, which is described in section 3.4. First we use the static droplet case to evaluate spurious currents and pressure prediction of this method compared to GFM and CSF. Next, the case of capillary wave relaxation is simulated to assess the efficiency of each of the implementation methods.

4.3.1 Static droplet

The ability of the decoupled pressure implementation of GFM to resolve the surface tension force and predict capillary pressure is studied. As was explained, GFM is used to capture surface tension force, however the capillary pressure is separated form other pressures by decomposing the dynamic pressure. For this simulation, the mesh domain measures $10cm \times 10cm$ and is comprised of uniformly distributed cells measuring $\Delta x = 1mm$. An initial droplet radius of $R_d = 25mm$ is initialized using interface reconstruction technique to avoid initial relaxation effects on simulation. The simulation time step is set to $\Delta t = 0.1\Delta x$. The physical properties for the droplet (liquid phase) are $\rho_l = 10$ and $1000kg/m^3$, $\mu_l = 0.001kg/ms$, and for the surrounding gas phase are $\rho_g = 1kg/m^3$, $\mu_g = 10^{-5}kg/ms$, with $\sigma = 0.05kg/s^2$. The numerical pressure solution can be compared with the analytical value by the 2D Young-Laplace equation as given in Eq.4.1.

As shown in Table 4.4, the maximum and average velocity (U_{max}, U_{ave}) are compared for different methods. The spurious currents generated by DPM are of the same order of magnitude as GFM, while both methods compute less artificial velocities relative to CSF. Comparison of the pressure error norms shows that DPM and GFM are in good agreement with the analytical pressure, and there is no considerable discrepancy between the two methods. This study proves that the DPM implementation still delivers good results in terms of pressure prediction and spurious currents generation.

Table 4.4: Parasitic currents and pressure comparison (at 50 time steps) between CSF, GFM and DPM.

Method	ρ_l/ρ_g	$U_{max}[m/s]$	$U_{ave}[m/s]$	L_1	L_2
A-CLSVOF/CSF	10	0.22	$3.1e-3$	0.05	0.13
	1000	0.51	$5.5e-3$	0.038	0.17
A-CLSVOF/GFM	10	$6.6e-3$	$2.8e-4$	$2.5e-3$	$4.9e-3$
	1000	$3.7e-4$	$1.32e-5$	$3.5e-3$	$7.2e-3$
DP-A-CLSVOF/GFM	10	$3.9e-3$	$1.9e-4$	$2.7e-3$	$5.1e-3$
	1000	$3.9e-4$	$1.35e-5$	$3.7e-4$	$6.6e-3$

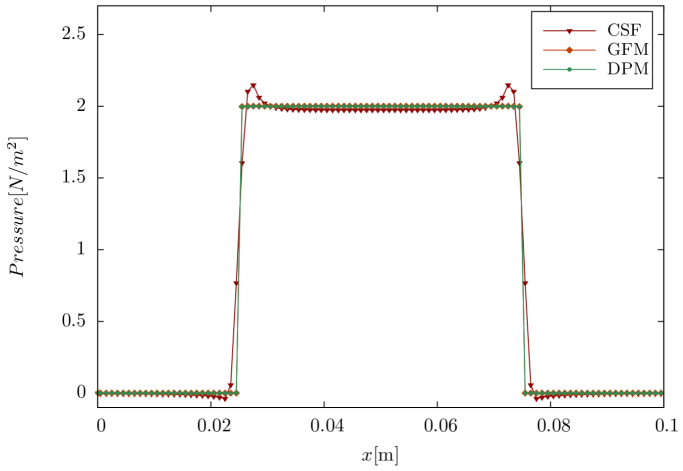

Figure 4.12: Comparison of pressure distributions at centerline for different methods.

4.3.2 Capillary wave relaxation

The capillary wave relaxation case is utilized to assess the efficiency of DPM technique in terms of the number of correction iterations in PISO loop. As was described before, PISO loop requires the number of iterations, N_C, to correct the velocity and pressure prediction. This number is recommended to be equal to or higher than 3 by many researchers [31] for the base PISO loop. Therefore, we study the effect of the correction number, N_C, in our simulation. The present method is tested using the same properties as in section 4.1.2 and is compared to the analytical solution for the wave amplitude versus time. The simulation domain is discretized as 33×33 and the capillary amplitude is plotted versus time in Fig.4.13. The results are plotted with different correction number, N_C, for both base PISO and DPM implementation. Fig.4.13 demonstrates that DPM delivers good result

even with one iteration $N_c = 1$. While the A-CLSVOF/GFM method needs at least three iterations to be roughly as accurate as DPM with one iteration. It proves that the DPM is substantially more efficient that the basic GFM solver.

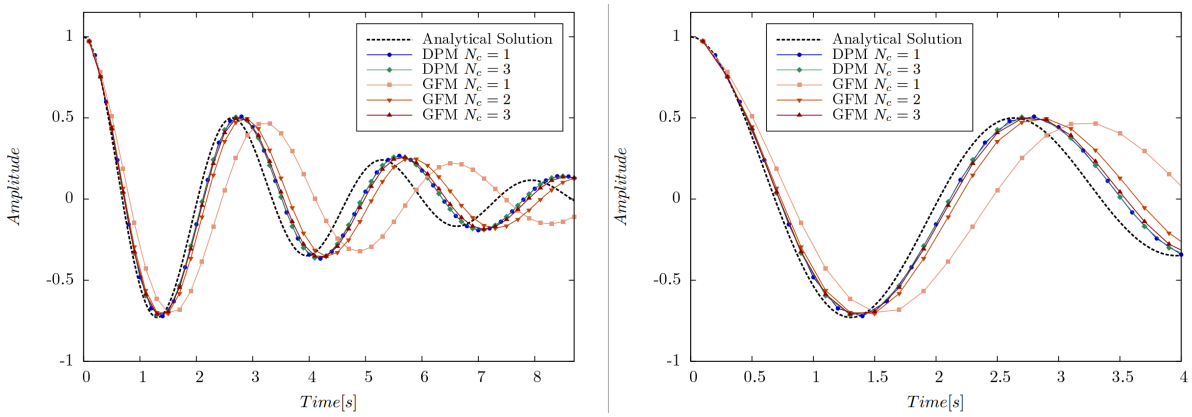

Figure 4.13: Comparison of DPM and segregated GFM in number of iteration for the case of capillary wave relaxation. N_c represents number of correction in PISO loop.

4.4 Oil jet simulation

In this section, oil jet simulation for various flow and fluid parameters are presented. First, the oil jet simulations are presented in a quiescent continuum phase which forms a straight jet. For low Reynolds numbers, we have capillary (dripping) jets as we discussed in section 2.2.2, which are compared with the experimental results. For higher injection velocities, jetting modes are captured to compare the breakup length with reported experimental works. Also, the simulations for are presented for high Reynolds number straight jets, where atomization breakup modes exist.

Subsequently, the oil jet in cross-flow water is reported for different modes of breakup for a combination of non-dimensional numbers. The effect of flow and fluid properties are studied using non-dimensional numbers such as Reynolds number, Re, Weber number, We, momentum ratio, J, and viscosity ratio, β. A regime map of breakup modes is presented for a wide range of Weber number and viscosity ratio.

4.4.1 Oil jet in quiescent water

To evaluate the accuracy of the two-phase flow solver, straight oil jets with different injection velocities (different Reynolds numbers) are simulated. The oil jet simulations are categorized according to breakup modes such as dripping, jetting, and atomization. For each mode of breakup, a few are simulated and compared to available experimental and numerical results reported in the literature. Non-dimensional numbers present different flow and fluid properties in this study. The jet Reynolds number, Re_j, is defined as the ratio of inertial force to viscous force, while the jet Weber number, We_j, is the ratio between the inertial force and the surface tension force. Reynolds and Weber numbers are formulated as:

$$Re_j = \frac{\rho_j U_j D_n}{\mu_j} \tag{4.7}$$

$$We_j = \frac{\rho_j U_j^2 D_n}{\sigma} \tag{4.8}$$

Where U_j is the jet injection velocity, D_n is nozzle diameter, μ_j is oil viscosity, ρ_j is oil density and σ is surface tension coefficient. In the dripping case, the capillary forces allow droplets to

form and pinch off. Injection velocity and the associated jet inertia are is not enough to form a jet, and droplets break up near the nozzle. In order to evaluate the accuracy of the solver, a case with flow properties as $Re_j = 19.8$, $We_j = 7.5e-3$ from a nozzle diameter of $D_n = 9.4mm$ is sumlated. The oil type chosen is Kerosene with properties as listed in Table 4.5. Fig. 4.14 shows the results of the current study compared with the reported simulation result of Homma et al. [56] and the experimental work of Song et al. [55]. The comparison shows that the unsteady simulation of Kerosene droplets in water is qualitatively in good agreement with the reported results. This verifies that the solver is capable of simulating capillary dominant flows such as dripping jets.

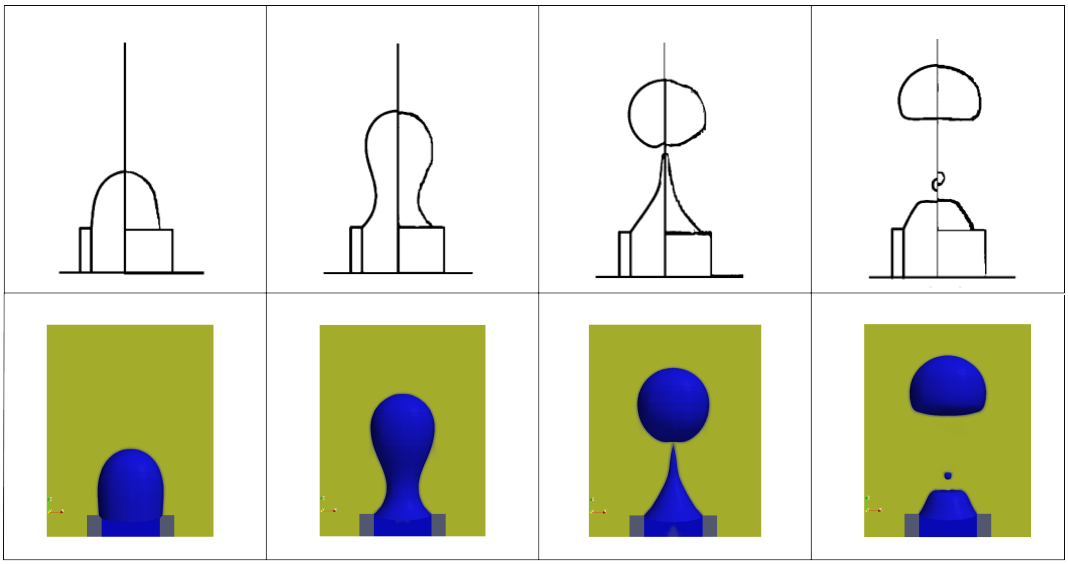

Figure 4.14: Comparison of present study simulation (bottom row) with respect to the result of Homma et al. (top row, left sides) and experiment Song et al. (top row, right sides).

In the jetting mode, the experimental studies of oil spill by Masutani [13] at the University of Hawaii are used for comparison. As listed in Table 4.6, different cases are simulated to compare

the predicted breakup length, L_b, with reported experimental results. Simulations are conducted in the axisymmetric domain, for an oil nozzle diameter is $5mm$. Three different crude oil types are simulated for a range of Reynolds numbers. Properties of three oil types are given in Table 4.5 according to [13]. Also, case 1 is qualitatively compared with the experiment in Fig. 4.15. According to Table 4.6, the captured breakup length, which is measured as the average values over time, compare well with experimental value reported by Masutani [13]. Considering the transition in simulation, the average value is within the margin of 10%.

Table 4.5: Properties of different oil types used in our simulation.

Oil type	$\rho[kg/m^3]$	$\mu[Pa.s]$	$\sigma[N/m]$
Platform Gail	992	0.196	0.025
Genesis	877	0.018	0.025
Heptane	683	$3.9e-4$	0.026
Mars TLP	882	0.024	0.025
Kerosene	890	0.0023	0.036

Also, a jetting case reported by Peng et al. [69] is simulated with the following properties: $\rho_j = 895kg/m^3$ $\mu_j = 0.179kg/ms$ and $\sigma = 0.062N/m$. Oil injects into the domain from nozzle $D_n = 0.12mm$ with injection velocity of $U_j = 1.61m/s$. In Fig. 4.16, the predicted density contours are seen to be in good agreement with the reported experimental data.

Table 4.6: Present study length of breakup L_b compared to result reported by reported experiments.

case #	Oil type	$U_j[m/s]$	Re	We	$L_b[cm]$ Experiment [13]	$L_b[cm]$ Present study
1	Platform Gail	0.115	3.8	2.36	16.1	17
2	Platform Gail	0.619	20.7	68.03	10.6	11.5
3	Genesis	0.252	66.9	10.7	3.0	3.1
4	Genesis	0.637	169	6.85	8.1	7.6
5	Mars TLP	0.145	30.1	3.57	10	11.1

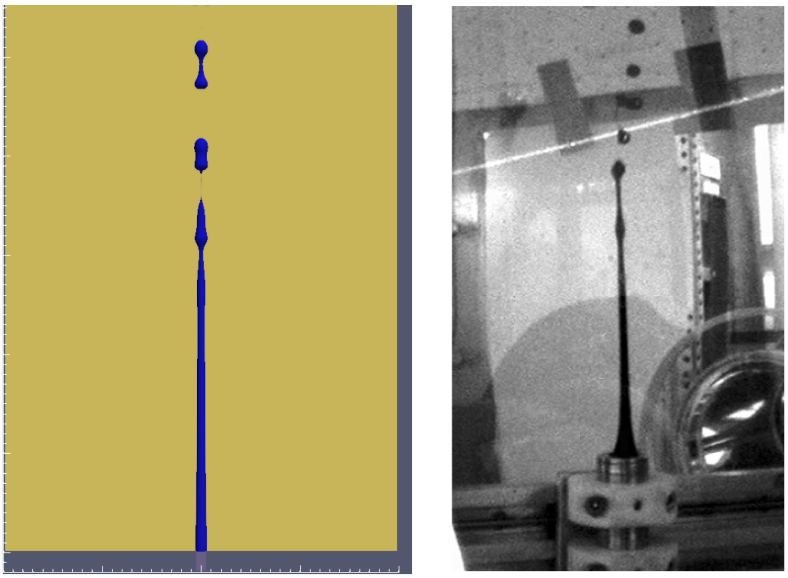

Figure 4.15: Comparison of capillary jet simulation (axisymmetric jetting breakup mode) of this study (left) with reported experimental result (right).

For higher Reynolds numbers, oil is discharged with high velocity and oil column was atomized. A 3D cylinder is utilized for the computational domain and a structured grid is generated for a more precise simulation. The nozzle diameter is 5mm at the bottom center of cylinder which features height and radius of 250mm and 50mm respectively. For this simulation, 10$million$ cells were used. Platform Gail is assumed to be the oil type (Table 4.5) in this simulation. Two cases are presented in Fig.4.17 with Reynolds number of 48 and 188, and Weber numbers of 335 and 1340 respectively. It is clear that for higher Reynolds numbers, the oil jet experiences a higher aerodynamic force, and instabilities are initiated near the injection point. High momentum interacting with surface tension and viscosity forces leads to atomization of the oil column. In particular for higher Reynolds number, the atomization mode is dominant and the jet breaks up faster into smaller scale droplets.

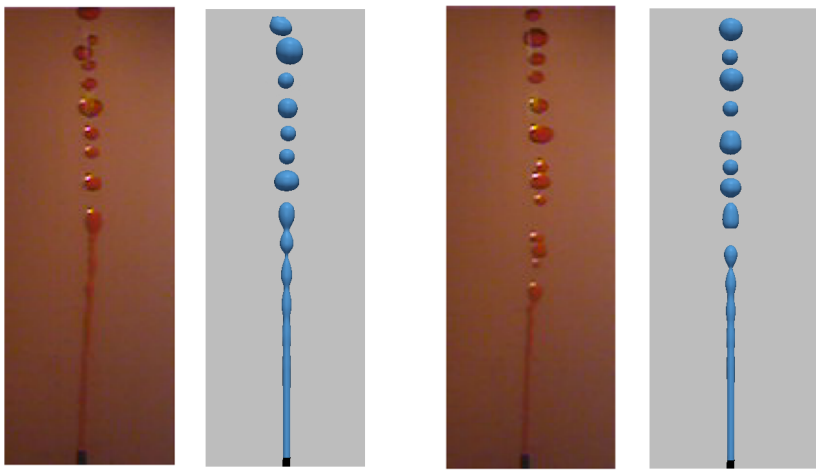

Figure 4.16: Qualitative validation of our jetting mode simulation (second and fourth from left) compared to empreimental (fisrt and third from left) results by Peng et al.

Most common hydrodynamic instabilities present in the atomization phenomenon are Rayleigh-Taylor instability, Rayleigh-Plateau instability, and Kelvin-Helmholtz instability. Rayleigh-Taylor instability occurs when one fluid accelerates and penetrates into another fluid with a different density. When two fluids move at different speeds, the relative velocity (velocity component tangential to the interface) induces vorticity at the interface. As a result, the interface becomes an unstable vortex sheet. This is called Kelvin-Helmholtz instability. Any fluid desires to be in the minimum energy state. Therefore, ligaments or any fluid columns deform such that the surface energy is minimized. Such deformation results in ligaments or columns to break into multiple droplets of the smaller total area. This phenomenon is called Rayleigh-Plateau instability. This phenomenon can be alternatively explained using the curvature variation of the perturbed ligament. This will result in pressure variation (from Young-Laplace Equation) along the ligament, creating a pressure gradient driven flow which ultimately becomes unstable and breakup into small droplets.

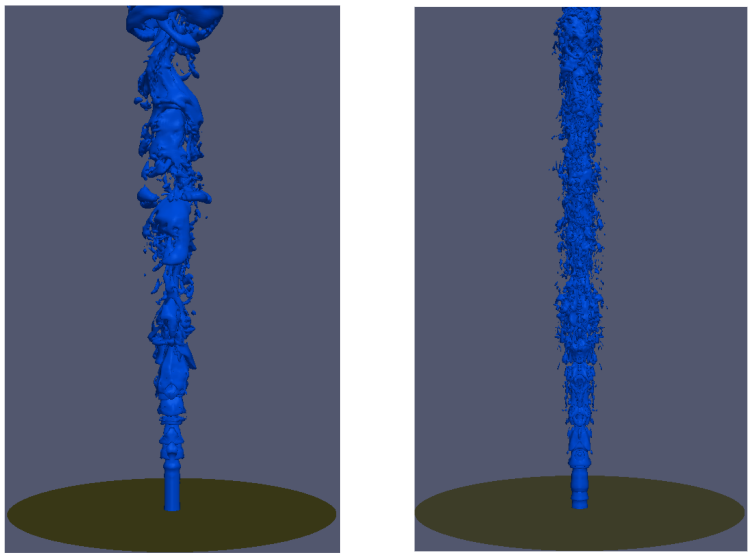

Figure 4.17: High Reynolds straight oil jet (atomization) simulation result for different injection velocities.

4.4.2 Oil jet in cross-flow

Considering water currents in seas, cross flow oil spill is more likely to occur in a real situation. Therefore we study the oil jet behavior in cross flowing water to characterize different modes of breakup for a wide range of non-dimensional numbers. The schematic view of the computational domain for simulation is depicted in Fig.4.18, in which nozzle diameter is fixed $D_n = 5mm$. Length, height and width of the computational domain are $L = 20cm$, $H = 10cm$ and $W = 6cm$ respectively, while the computational domain is uniformly discretized with $\approx 2.8million$ cells as grid size is $Dx = Dy = Dz = 0.4mm$. We have uniform cross-flow velocity U_c and parabolic oil in-

jection velocity U_j set at each inlet boundaries. For this study we need additional non-dimensional numbers to represent the cross-flow effects. Therefore, we present the cross-flow Reynolds number and momentum ratio which are defined as:

$$Re_c = \frac{\rho_c U_c D_n}{\mu_c} \tag{4.9}$$

$$J = \frac{\rho_j U_j^2}{\rho_c U_c^2} \tag{4.10}$$

The momentum ratio J presents the effect of cross-flow hydrodynamics on the penetrating oil jet. Initially, different breakup modes are studied in cross-flow jet. Kerosene is used as the oil type and tap-water is the crossing water. The oil injects with parabolic velocity profile from a nozzle at the bottom of domain (Fig.4.18). Different combinations of jet Reynolds number and momentum ratio are simulated to capture different breakup modes as depicted in Fig. 4.19. Also, the time evolution of each breakup mode is presented in Fig. 4.20.

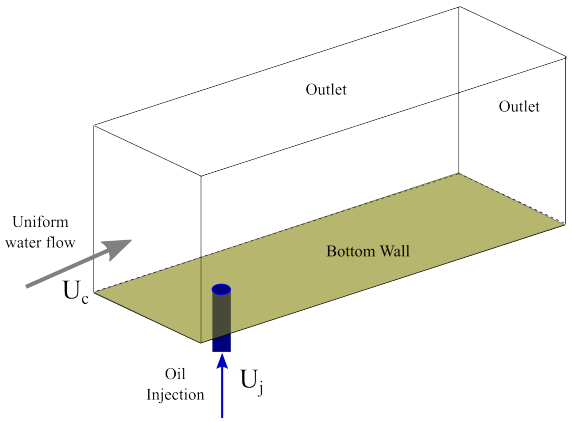

Figure 4.18: Schematic view of the considered domain for cross flow simulation.

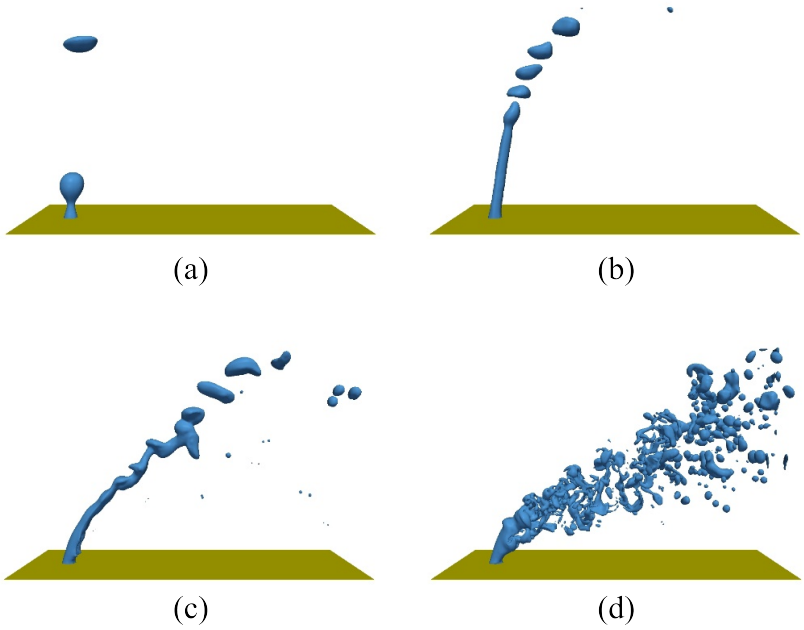

Figure 4.19: Different modes of breakup for an oil jet in cross-flow water for $J = 3.5$ a) dripping $Re_j = 70$ b) axisymmetric jetting $Re_j = 350$ c) asymmetric jetting $Re_j = 760$ d) atomization $Re_j = 2200$.

For very low Re_j, the oil jet is characterized as dripping mode (capillary jet) in Fig.4.19(a), where the cross-flow effects on droplet formation and separation are negligible. Higher injection velocity, however, generates enough inertial force to form a jet column and penetrate into the cross-flow (fig. 4.19(b), where the capillary waves are still the dominant breakup mechanism. The near-axisymmetric breakup changes into an asymmetric pattern when shear flow induced by cross-flow destabilizes the penetrating jet (Fig. 4.19(c)). Eventually, at very high Re_j the oil jet atomizes near the injection point (Fig. 4.19(d)). At this high cross-flow, ligaments appear, which break up into smaller droplets even at the lower portion of the physical domain.

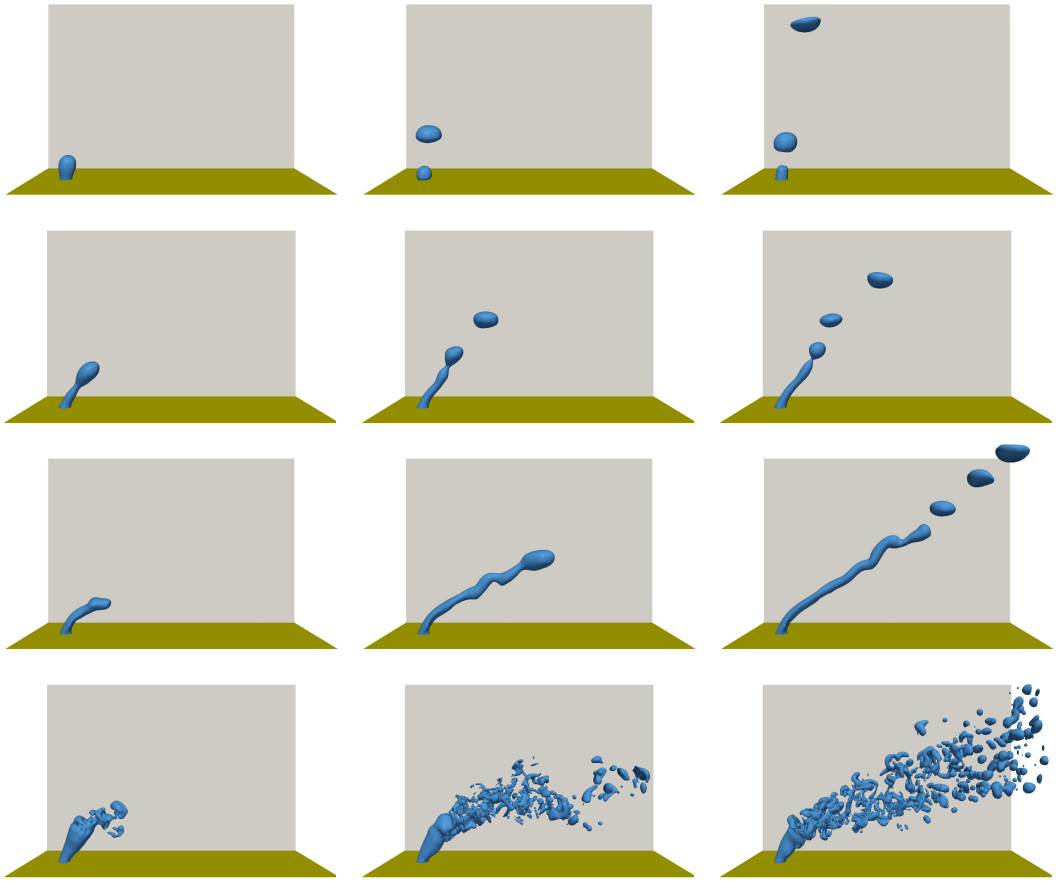

Figure 4.20: Time evolution of different modes of breakup for an oil jet in cross-flow water: dripping, axisymmetric jetting, asymmetric jetting and atomization.

Fig. 4.21 shows the effect of the momentum ratio on jet trajectory for $Re_j = 968$ and $We = 25$. High J indicates that the jet momentum is relatively high and the cross-flow inertia is smaller. As is expected, a decrease in J value leads to a decrease in the breakup height as cross-flow becomes stronger. This figure shows that the breakup mode does not change by changing the momentum ratio for $Re_j = 968$. However, later the study on effect of momentum ratio on breakup mode reveals that depending on Re_j, the breakup mode could change for different J (Fig.4.22).

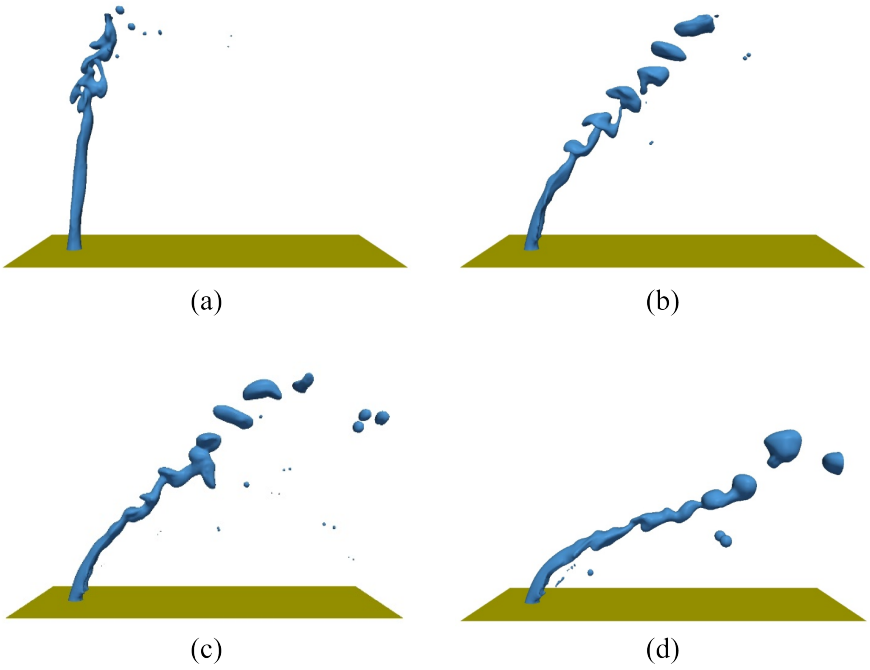

Figure 4.21: Effect of cross-flow momentum of discharged oil for $Re_j = 968$, $We = 25$: a) $J = 22.4$ b) $J = 9.9$ c) $J = 5$ d) $J = 3.5$.

A regime map of different breakup modes is presented for a range of Re_j and J in Fig. 4.22. For the given range, an increase in J leads to a change in the breakup mode from axisymmetric jetting to asymmetric jetting at fixed Re_j as seen earlier in Fig. 4.19. This confirms that for a fixed Reynolds number, if the jet could penetrate into the cross-flow of higher J, shear forces would initiate asymmetric instabilities on the jet column. For high Re_j, high cross-flow (low J) leads to atomization of the discharged oil. It can be seen from the flow regime map that as J increases, the axisymmetric jetting transition to asymmetric jetting earlier. For the highest J of 5, the flow regime stays in the asymmetric jetting mode the longest before completely atomizing. As J decreases, i.e.,

as the coss-flow increases, atomization begins earlier. For example, for $J = 0.5$ atomization occurs much earlier at $Re_j = 800$.

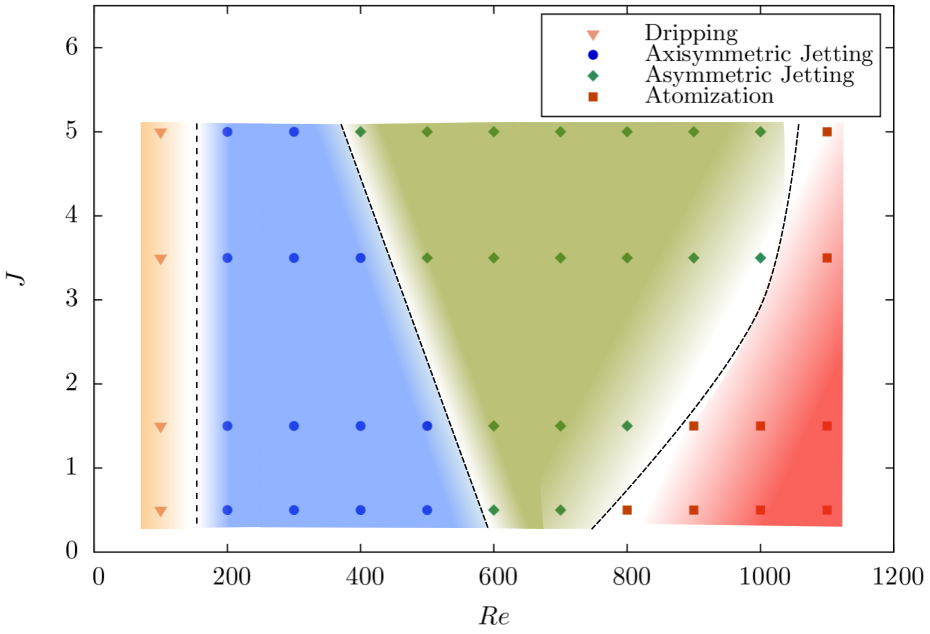

Figure 4.22: Regime map of different modes of breakup for an oil jet in cross-flow water based on mpmentum ratio J and jet Rynolds number Re_j.

In order to study the effect of jet viscosity, four real oil types such as Heptane, Kerosene, Mars TLP and Platform Gail (last two oils are crude oils) listed in Table 4.5 are chosen. Velocities of oil jet and cross-flow are fixed as $U_j = 0.5m/s$ and $U_c = 0.2m/s$ respectively. Different oil types result in different injection Reynolds and Weber numbers as are reported in Fig. 4.23. For low viscous oil (Heptane and Kerosene), jet transitions to atomization phase and stronger instabilities break down the jet column. Breakup height and distance are relatively short, and a wide rage of droplets are separated from the jet column. For about the same Weber number with a reduced

Reynolds number, the jet column is seen t be broken at a distance, forming ligaments (Fig.4.23(b)). As the oil viscosity is further increased for the crude oil like Mars TLP (Fig.4.23(c)) and Platform Gail (Fig.4.23(d)), then is general resistance to the developing instabilities, as the breakup point is prolonged to well outside the computational domain.

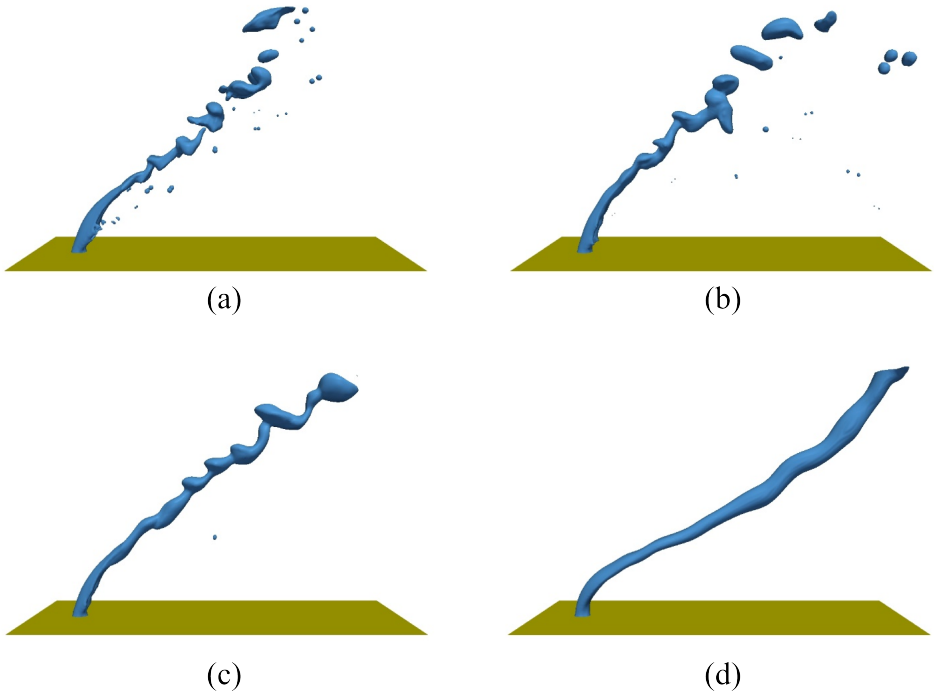

Figure 4.23: Effect oil viscosity on breakup dynamics by cosidering four real oil types: a) Heptane $Re_j = 4300$, $We_j = 32.5$ b) Kerosene $Re_j = 960$, $We_j = 30.1$ c) Mars TLP $Re_j = 91.8$, $We_j = 44$ d) Platform Gail $Re_j = 15.4$, $We_j = 46.1$.

Next, the role of oil surface tension is investigated for the same jet Reynolds numbers. A wide range of surface tension coefficients $0.02 < \sigma[N/m] < 0.05$ are considered for a fixed jet viscosity and density (Kerosene oil properties in Table 4.5). As is shown in Fig. 4.24, the jet is continuous

with late breakup for low Weber numbers (high surface tension coefficient). For higher jet Weber numbers We_j, the inertial force is stronger than the opposing surface tension force and leads to an unstable cylindrical jet breaking up under growing K-H and capillary instabilities.

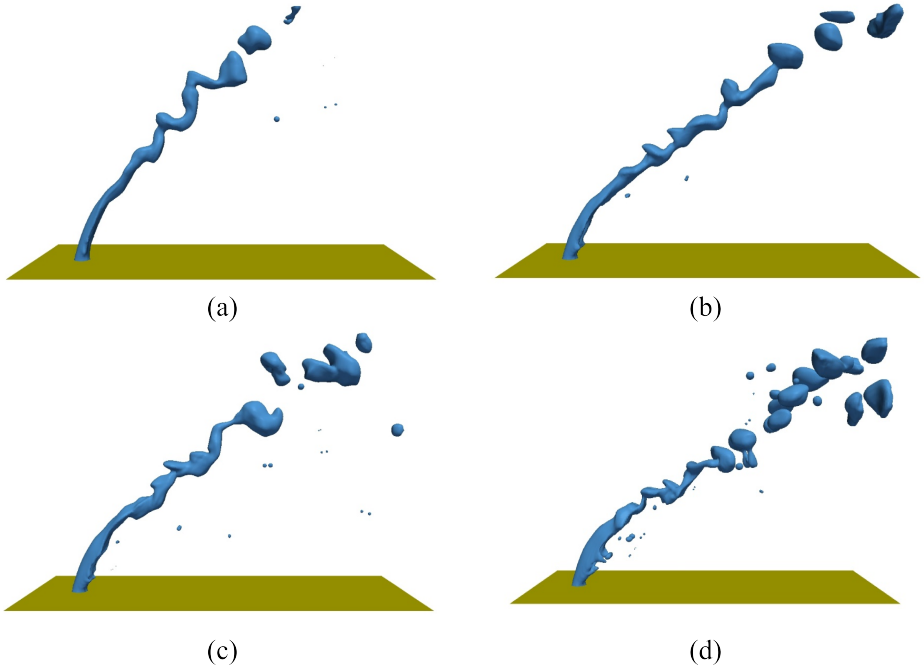

Figure 4.24: Effect oil surface tension on jet breakup pattern by considering Kerosene oil with different surface tension coefficients and accordingly Weber numbers: a) $We_j = 22.25$ b) $We_j = 27.81$ c) $We_j = 37.08$ d) $We_j = 55.62$. For all the cases Reynolds is the same as $Re_j = 968$.

These simulations reveal how the breakup modes are influenced by viscosity ratio ($\beta = \mu_j/\mu_c$) and jet Weber number We_j. A regime map of breakup modes is presented for a wide range of We_j and β at two momentum ratios $J = 3.5$ and $J = 2$ in Fig. 4.25. The viscosity ratio β is changed by adjusting different oil types, and the surface tension is fixed $\sigma = 0.035$ to remove its effect on our simulation. Also, the jet Weber number We_j is adjusted by altering the oil injection velocity U_j.

Fig. 4.25 shows the transition from dripping to jetting and atomization modes as Weber number increases. For a considerable range of Weber numbers, higher β resulted in a change of breakup mode with each regime persisting longer. For instance, at $We_j = 8.5$ asymmetric jetting changed into axisymmetric jetting for higher β. In the same manner, lower deterring viscous force induced more instabilities where asymmetric jetting shifts into atomization mode for high We_j. Study of momentum ratio J effect on the regime map reveals that low J (higher cross-flow momentum) resulted into a further shift up in transition lines.

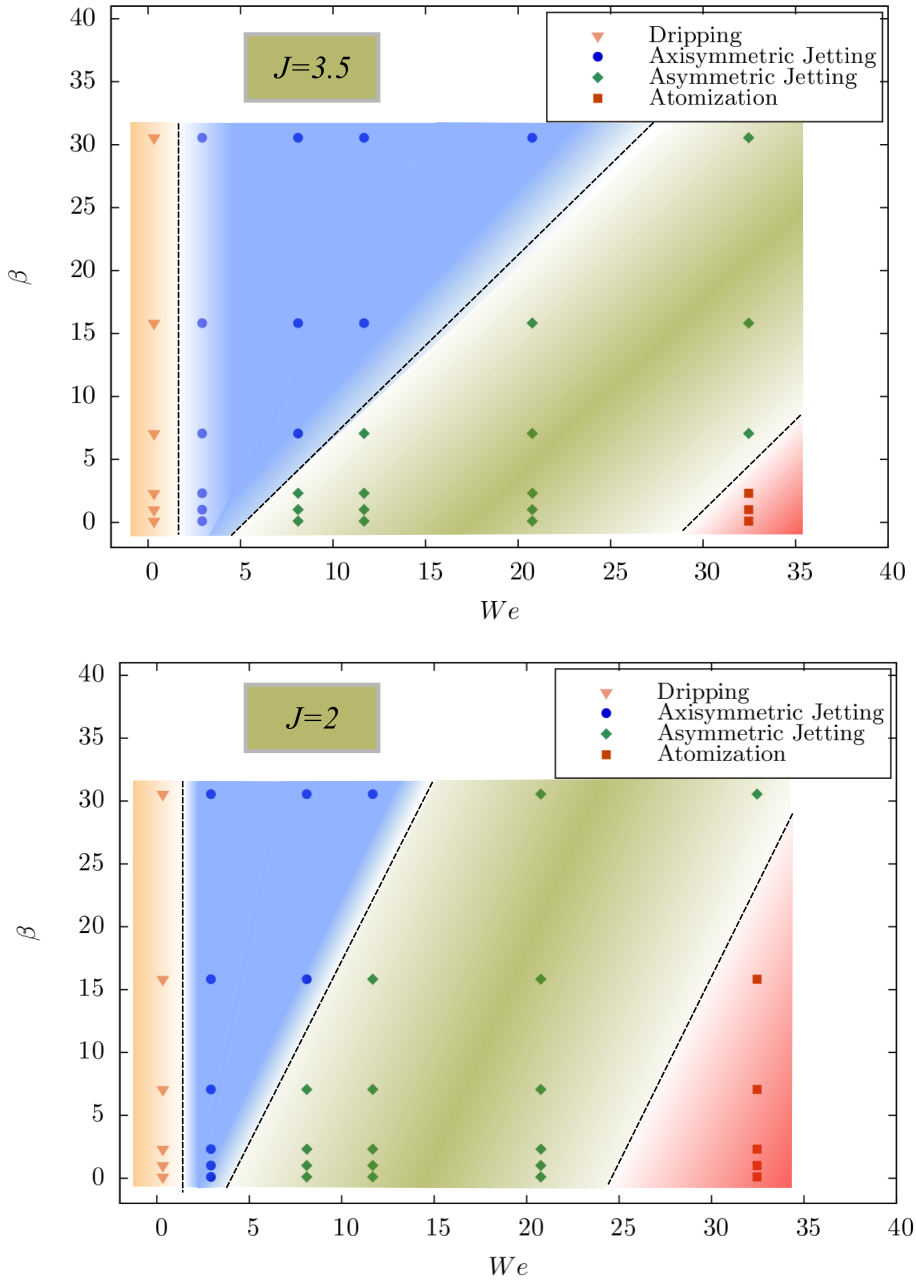

Figure 4.25: Regime map of different modes of breakup for a wide range of We_j and $\beta = mu_j/\mu_c$, for different momentum ratios, $J = 2$ and $J = 3.5$.

CHAPTER 5
CONCLUSION

A two-phase flow model, Arithmetic-Coupled Level Set Volume of Fluid method, implementing concepts from recent literature and innovations that promote mass conservation during reinitialization and filtering to smooth interface normal orientation is presented. The numerical formulation of this model, along with up/downwinding discretization using the Hamilton-Godunov function results in an accurate, efficient and robust reinitialization technique to produce a Level Set function consistent with the mass conservative volume fraction field. This function allows for complete autonomy when choosing not only when a first or second order accurate spatial discretization is appropriate, but where the appropriate up/downwinding direction lies for any cell.

The resulting interface normal undergoes filtering to eliminate any erratic variations along the interface resulting from the coarse volume fraction initialization on the modeled grid scale; filtering redistributes interface normal orientation to be more uniform in their inclination changes along any given length of the interface. Finally, overall efficiency and accuracy of the present method was improved via the addition of Level Set advection where the initial guess for the reinitialization procedure becomes better conditioned and close to the converged result. Multiple canonical test cases are presented in order to demonstrate the current methods ability to efficiently resolve capillary forces.

For the static droplet case, this algebraic formulation considerably reduces the parasitic currents, even for coarse grids when compared to the Volume of Fluid method and method of [61]. Results for a capillary waves relaxation produced errors comparable to the other more rigorous methods such as Gerlach et al. [64] and the well-known Front Tracking method of Poppinet et al. [62]. Our simulation results for the standard Rayleigh-Taylor non-linear instability have been compared to results reported by other researchers Zuzio et al. [65] and indicates excellent agreement at various solution times. This study also serves as a means of benchmarking the addition of LS advection. Results demonstrate a reduction in simulation time of $\sim 45\%$ while improving the converged steady state error due to the improvement to the initial guess of the distance function provided by advection.

As a final case, simulation results for droplet impact on a liquid pool were compared to the Volume of Fluid method as well as experimental results. The grid study shows that the current method reaches grid independence on a grid more than twice the size of the grid required by the Volume of Fluid method while modeling the experimental result with exceptional accuracy, especially when compared to the Volume of Fluid Method. This present model also demonstrates its capabilities in modeling capillary flows due to its robustness in handling topology through the use of the Hamilton-Godunov function and the use of second order accurate discretization schemes for space and time. Not only does the method produce an accurate result, but the inclusion of Level-Set advection drastically reduces the solution time, making its appeal for the solution of many complex interfacial engineering problems.

As the next phase in developing the two-phase solver, the ghost fluid method (GFM) is utilized to implement the sharp capillary, hydrostatic, and viscous forces in the discretization of the pressure terms in the momentum and pressure equations in the PISO loop while using the A-CLSVOF method for interface tracking. The GFM produces a sharp and accurate pressure jump compared to the traditional CSF implementation with A-CLSVOF. The discretization of the surface tension force reduces the presence of spurious currents when compared to the CSF method, especially for higher density ratios as the sharp density transition is provided by GFM. The interaction of viscous and capillary forces is proven to be consistent with theoretical results for capillary wave. For the linear two-layer shear flow, GFM sharp treatment of the viscosity captured the velocity gradient across the interface and removed the diffusion of the viscous stresses caused by the discontinuous material properties. Finally, the combination of all GFM improvements proposed in this study are compared to experimental findings of terminal velocity for a gaseous bubble rising in a viscous fluid. GFM outperforms CSF with errors of 4.6% and 14.0% respectively.

Also, new implementation of PISO loop is introduced, which decouples pressure into two components. P_1 Presents interfacial forces at transition region and P_2 accounts for the rest of flow pressure. This modified momentum solution, which is named as decoupled pressure method (DPM), separates pressure Poisson equation into two laplacian solution. First, P_1 is solved and passed to velocity predictor, then the predicted velocity induces dynamic pressure to P_2 poisson solution. The DPM technique is assessed by static droplet and capillary wave cases. The static droplet simulation reveals that DPM is as as accurate as GFM method in capillary pressure prediction and spurious current generation. Capillary wave case demonstrates that DPM delivers good

result even with one PISO loop iteration $N_c = 1$. While the A-CLSVOF/GFM method needs at least three iterations to be roughly as accurate as DPM with one iteration. It proves that the DPM is substantially more efficient that the basic GFM solver.

The breakup regimes of a circular oil jet injected into the water cross-flow were investigated numerically. Four breakup modes were observed with increasing jet Reynolds number: dripping, axisymmetric jetting, asymmetric jetting and atomization. The asymmetric jetting regime, which is dominated by Kelvin-Helmholtz instability, occurs for a wider range of Reynolds numbers compared with the straight jet, since continuous phase momentum initiates KH instability. A regime map of different breakup modes for a wide range of We_j amd β is developed for different momentum flux ratio. For a considerable range of Weber numbers, higher β resulted in a change of breakup mode with each regime persisting longer. In the same manner, lower deterring viscous force induced more instabilities where asymmetric jetting shifts into atomization mode for high We_j. Study of momentum ratio J effect on the regime map reveals that low J (higher cross-flow momentum) resulted into a further shift up in transition lines.

LIST OF REFERENCES

[1] E. Villermaux, P. Marmottant, and J. Duplat, "Ligament-mediated spray formation," *Physical review letters*, vol. 92, no. 7, p. 074501, 2004.

[2] O. Desjardins, J. McCaslin, M. Owkes, and P. Brady, "Direct numerical and large-eddy simulation of primary atomization in complex geometries," *Atomization and Sprays*, vol. 23, no. 11, 2013.

[3] C. E. Brennen and C. E. Brennen, *Fundamentals of multiphase flow*. Cambridge university press, 2005.

[4] G. Tryggvason, R. Scardovelli, and S. Zaleski, *Direct numerical simulations of gas–liquid multiphase flows*. Cambridge University Press, 2011.

[5] D. S. Dandy and L. G. Leal, "Buoyancy-driven motion of a deformable drop through a quiescent liquid at intermediate reynolds numbers," *Journal of Fluid Mechanics*, vol. 208, pp. 161–192, 1989.

[6] S. O. Unverdi and G. Tryggvason, "A front-tracking method for viscous, incompressible, multi-fluid flows," *Journal of computational physics*, vol. 100, no. 1, pp. 25–37, 1992.

[7] C. W. Hirt and B. D. Nichols, "Volume of fluid (vof) method for the dynamics of free boundaries," *Journal of computational physics*, vol. 39, no. 1, pp. 201–225, 1981.

[8] S. Osher and J. A. Sethian, "Fronts propagating with curvature-dependent speed: algorithms based on hamilton-jacobi formulations," *Journal of computational physics*, vol. 79, no. 1, pp. 12–49, 1988.

[9] B. Nadiga and S. Zaleski, "Investigations of a two-phase fluid model," *arXiv preprint comp-gas/9511003*, 1995.

[10] V. Dyadechko and M. Shashkov, "Moment-of-fluid interface reconstruction," *Los Alamos Report LA-UR-05-7571*, 2005.

[11] A. Bourlioux, "A coupled level-set volume-of-fluid algorithm for tracking material interfaces," in *proceedings of the 6th international symposium on computational fluid dynamics, Lake Tahoe, CA*, vol. 15, 1995.

[12] M. Jemison, E. Loch, M. Sussman, M. Shashkov, M. Arienti, M. Ohta, and Y. Wang, "A coupled level set-moment of fluid method for incompressible two-phase flows," *Journal of Scientific Computing*, vol. 54, no. 2-3, pp. 454–491, 2013.

[13] S. M. Masutani and E. E. Adams, "Experimental study of multi-phase plumes with application to deep ocean oil spills," *Final Report*, 2001.

[14] W. F. Noh and P. Woodward, "Slic (simple line interface calculation)," in *Proceedings of the fifth international conference on numerical methods in fluid dynamics June 28–July 2, 1976 Twente University, Enschede*. Springer, 1976, pp. 330–340.

[15] D. L. Youngs, "Time-dependent multi-material flow with large fluid distortion," *Numerical methods for fluid dynamics*, 1982.

[16] N. Ashgriz and J. Poo, "Flair: Flux line-segment model for advection and interface reconstruction," *Journal of computational physics*, vol. 93, no. 2, pp. 449–468, 1991.

[17] W. J. Rider and D. B. Kothe, "Reconstructing volume tracking," *Journal of computational physics*, vol. 141, no. 2, pp. 112–152, 1998.

[18] J. E. Pilliod, *An analysis of piecewise linear interface reconstruction algorithms for volume-of-fluid methods*. U. of Calif., Davis., 1992.

[19] Y. Renardy and M. Renardy, "Prost: a parabolic reconstruction of surface tension for the volume-of-fluid method," *Journal of computational physics*, vol. 183, no. 2, pp. 400–421, 2002.

[20] J. López, J. Hernández, P. Gómez, and F. Faura, "A volume of fluid method based on multidimensional advection and spline interface reconstruction," *Journal of Computational Physics*, vol. 195, no. 2, pp. 718–742, 2004.

[21] J. E. Pilliod Jr and E. G. Puckett, "Second-order accurate volume-of-fluid algorithms for tracking material interfaces," *Journal of Computational Physics*, vol. 199, no. 2, pp. 465–502, 2004.

[22] J. Hernández, J. López, P. Gómez, C. Zanzi, and F. Faura, "A new volume of fluid method in three dimensionspart i: Multidimensional advection method with face-matched flux polyhedra," *International Journal for Numerical Methods in Fluids*, vol. 58, no. 8, pp. 897–921, 2008.

[23] M. Owkes and O. Desjardins, "A computational framework for conservative, three-dimensional, unsplit, geometric transport with application to the volume-of-fluid (vof) method," *Journal of Computational Physics*, vol. 270, pp. 587–612, 2014.

[24] J. Brackbill, D. B. Kothe, and C. Zemach, "A continuum method for modeling surface tension," *Journal of computational physics*, vol. 100, no. 2, pp. 335–354, 1992.

[25] B. Lafaurie, C. Nardone, R. Scardovelli, S. Zaleski, and G. Zanetti, "Modelling merging and fragmentation in multiphase flows with surfer," *Journal of Computational Physics*, vol. 113, no. 1, pp. 134–147, 1994.

[26] M. M. Francois, S. J. Cummins, E. D. Dendy, D. B. Kothe, J. M. Sicilian, and M. W. Williams, "A balanced-force algorithm for continuous and sharp interfacial surface tension models within a volume tracking framework," *Journal of Computational Physics*, vol. 213, no. 1, pp. 141–173, 2006.

[27] M. Rudman, "Volume-tracking methods for interfacial flow calculations," *International journal for numerical methods in fluids*, vol. 24, no. 7, pp. 671–691, 1997.

[28] O. Ubbink, "Numerical prediction of two fluid systems with sharp interfaces," Ph.D. dissertation, University of London PhD Thesis, 1997.

[29] H. G. Weller, "A new approach to vof-based interface capturing methods for incompressible and compressible flow," *OpenCFD Ltd., Report TR/HGW/04*, 2008.

[30] H. G. Weller, G. Tabor, H. Jasak, and C. Fureby, "A tensorial approach to computational continuum mechanics using object-oriented techniques," *Computers in physics*, vol. 12, no. 6, pp. 620–631, 1998.

[31] S. S. Deshpande, L. Anumolu, and M. F. Trujillo, "Evaluating the performance of the two-phase flow solver interfoam," *Computational science & discovery*, vol. 5, no. 1, p. 014016, 2012.

[32] M. Sussman, P. Smereka, and S. Osher, "A level set approach for computing solutions to incompressible two-phase flow," *Journal of Computational physics*, vol. 114, no. 1, pp. 146–159, 1994.

[33] S. Osher and R. P. Fedkiw, "Level set methods: an overview and some recent results," *Journal of Computational physics*, vol. 169, no. 2, pp. 463–502, 2001.

[34] E. Olsson and G. Kreiss, "A conservative level set method for two phase flow," *Journal of computational physics*, vol. 210, no. 1, pp. 225–246, 2005.

[35] O. Desjardins, V. Moureau, and H. Pitsch, "An accurate conservative level set/ghost fluid method for simulating turbulent atomization," *Journal of Computational Physics*, vol. 227, no. 18, pp. 8395–8416, 2008.

[36] M. Sussman and E. G. Puckett, "A coupled level set and volume-of-fluid method for computing 3d and axisymmetric incompressible two-phase flows," *Journal of computational physics*, vol. 162, no. 2, pp. 301–337, 2000.

[37] M. Sussman, "A second order coupled level set and volume-of-fluid method for computing growth and collapse of vapor bubbles," *Journal of Computational Physics*, vol. 187, no. 1, pp. 110–136, 2003.

[38] T. Ménard, S. Tanguy, and A. Berlemont, "Coupling level set/vof/ghost fluid methods: Validation and application to 3d simulation of the primary break-up of a liquid jet," *International Journal of Multiphase Flow*, vol. 33, no. 5, pp. 510–524, 2007.

[39] R. P. Fedkiw, T. Aslam, B. Merriman, and S. Osher, "A non-oscillatory eulerian approach to interfaces in multimaterial flows (the ghost fluid method)," *Journal of computational physics*, vol. 152, no. 2, pp. 457–492, 1999.

[40] R. P. Fedkiw, T. Aslam, and S. Xu, "The ghost fluid method for deflagration and detonation discontinuities," *Journal of Computational Physics*, vol. 154, no. 2, pp. 393–427, 1999.

[41] X.-D. Liu, R. P. Fedkiw, and M. Kang, "A boundary condition capturing method for poisson's equation on irregular domains," *Journal of computational Physics*, vol. 160, no. 1, pp. 151–178, 2000.

[42] M. Kang, R. P. Fedkiw, and X.-D. Liu, "A boundary condition capturing method for multiphase incompressible flow," *Journal of Scientific Computing*, vol. 15, no. 3, pp. 323–360, 2000.

[43] J. Huang, P. M. Carrica, and F. Stern, "Coupled ghost fluid/two-phase level set method for curvilinear body-fitted grids," *International Journal for Numerical Methods in Fluids*, vol. 55, no. 9, pp. 867–897, 2007.

[44] M. Sussman, K. M. Smith, M. Y. Hussaini, M. Ohta, and R. Zhi-Wei, "A sharp interface method for incompressible two-phase flows," *Journal of computational physics*, vol. 221, no. 2, pp. 469–505, 2007.

[45] M. Aanjaneya, S. Patkar, and R. Fedkiw, "A monolithic mass tracking formulation for bubbles in incompressible flow," *Journal of Computational Physics*, vol. 247, pp. 17–61, 2013.

[46] K. Hayashi and A. Tomiyama, "Effects of numerical treatment of viscous and surface tension forces on predicted motion of interface," *The Journal of Computational Multiphase Flows*, vol. 6, no. 2, pp. 111–126, 2014.

[47] B. Lalanne, L. R. Villegas, S. Tanguy, and F. Risso, "On the computation of viscous terms for incompressible two-phase flows with level set/ghost fluid method," *Journal of Computational Physics*, vol. 301, pp. 289–307, 2015.

[48] V. Vukčević, H. Jasak, and I. Gatin, "Implementation of the ghost fluid method for free surface flows in polyhedral finite volume framework," *Computers & fluids*, vol. 153, pp. 1–19, 2017.

[49] B. J. Meister and G. F. Scheele, "Drop formation from cylindrical jets in immiscible liquid systems," *AIChE Journal*, vol. 15, no. 5, pp. 700–706, 1969.

[50] ——, "Prediction of jet length in immiscible liquid systems," *AIChE Journal*, vol. 15, no. 5, pp. 689–699, 1969.

[51] Y. Kitamura, "Stability of jets in liquid-liquid systems," *The Canadian Journal of Chemical Engineering*, vol. 62, no. 4, pp. 571–571, 1984.

[52] A. Bright, "Minimum drop volume in liquid jet breakup," *Chemical Engineering Research and Design*, vol. 63, pp. 59–66, 1985.

[53] H. Teng, C. Kinoshita, and S. Masutani, "Prediction of droplet size from the breakup of cylindrical liquid jets," *International Journal of Multiphase Flow*, vol. 21, no. 1, pp. 129–136, 1995.

[54] T. K. Das, "Droplet formation with single and multiple nodes from a liquid jet in immiscible liquids," *Atomization and Sprays*, vol. 7, no. 4, 1997.

[55] M. Song, S. Homma, K. Hong *et al.*, "Formation of oil drops discharged underwater," in *The Ninth International Offshore and Polar Engineering Conference*. International Society of Offshore and Polar Engineers, 1999.

[56] S. Homma, J. Koga, S. Matsumoto, M. Song, and G. Tryggvason, "Breakup mode of an axisymmetric liquid jet injected into another immiscible liquid," *Chemical engineering science*, vol. 61, no. 12, pp. 3986–3996, 2006.

[57] J. R. Richards, A. N. Beris, and A. M. Lenhoff, "Drop formation in liquid–liquid systems before and after jetting," *Physics of fluids*, vol. 7, no. 11, pp. 2617–2630, 1995.

[58] A. M. Lakdawala, V. H. Gada, and A. Sharma, "A dual grid level set method based study of interface-dynamics for a liquid jet injected upwards into another liquid," *International Journal of Multiphase Flow*, vol. 59, pp. 206–220, 2014.

[59] H. Rusche, "Computational fluid dynamics of dispersed two-phase flows at high phase fractions," Ph.D. dissertation, Imperial College London (University of London), 2003.

[60] F. Moukalled, L. Mangani, M. Darwish *et al.*, "The finite volume method in computational fluid dynamics," 2016.

[61] D. Hartmann, M. Meinke, and W. Schröder, "The constrained reinitialization equation for level set methods," *Journal of Computational Physics*, vol. 229, no. 5, pp. 1514–1535, 2010.

[62] C. Min, "On reinitializing level set functions," *Journal of computational physics*, vol. 229, no. 8, pp. 2764–2772, 2010.

[63] M. Sussman, E. Fatemi, P. Smereka, and S. Osher, "An improved level set method for incompressible two-phase flows," *Computers & Fluids*, vol. 27, no. 5-6, pp. 663–680, 1998.

[64] A. Albadawi, D. Donoghue, A. Robinson, D. Murray, and Y. Delauré, "Influence of surface tension implementation in volume of fluid and coupled volume of fluid with level set methods for bubble growth and detachment," *International Journal of Multiphase Flow*, vol. 53, pp. 11–28, 2013.

[65] M. Bardi and S. Osher, "The nonconvex multidimensional riemann problem for hamilton–jacobi equations," *SIAM Journal on Mathematical Analysis*, vol. 22, no. 2, pp. 344–351, 1991.

[66] D. Peng, B. Merriman, S. Osher, H. Zhao, and M. Kang, "A pde-based fast local level set method," *Journal of computational physics*, vol. 155, no. 2, pp. 410–438, 1999.

[67] A. Q. Raeini, M. J. Blunt, and B. Bijeljic, "Modelling two-phase flow in porous media at the pore scale using the volume-of-fluid method," *Journal of Computational Physics*, vol. 231, no. 17, pp. 5653–5668, 2012.

[68] S. Hardt and F. Wondra, "Evaporation model for interfacial flows based on a continuum-field representation of the source terms," *Journal of Computational Physics*, vol. 227, no. 11, pp. 5871–5895, 2008.

[69] M. Haghshenas, J. A. Wilson, and R. Kumar, "Algebraic coupled level set-volume of fluid method for surface tension dominant two-phase flows," *International Journal of Multiphase Flow*, vol. 90, pp. 13–28, 2017.

[70] R. I. Issa, "Solution of the implicitly discretised fluid flow equations by operator-splitting," *Journal of computational physics*, vol. 62, no. 1, pp. 40–65, 1986.

[71] A. Yoshizawa and K. Horiuti, "A statistically-derived subgrid-scale kinetic energy model for the large-eddy simulation of turbulent flows," *Journal of the Physical Society of Japan*, vol. 54, no. 8, pp. 2834–2839, 1985.

[72] S. Popinet and S. Zaleski, "A front-tracking algorithm for accurate representation of surface tension," *International Journal for Numerical Methods in Fluids*, vol. 30, no. 6, pp. 775–793, 1999.

[73] A. Prosperetti, "Motion of two superposed viscous fluids," *The Physics of Fluids*, vol. 24, no. 7, pp. 1217–1223, 1981.

[74] D. Gerlach, G. Tomar, G. Biswas, and F. Durst, "Comparison of volume-of-fluid methods for surface tension-dominant two-phase flows," *International Journal of Heat and Mass Transfer*, vol. 49, no. 3-4, pp. 740–754, 2006.

[75] D. Zuzio and J. Estivalezes, "An efficient block parallel amr method for two phase interfacial flow simulations," *Computers & Fluids*, vol. 44, no. 1, pp. 339–357, 2011.

[76] J. Lopez, J. Hernandez, P. Gomez, and F. Faura, "An improved plic-vof method for tracking thin fluid structures in incompressible two-phase flows," *Journal of Computational Physics*, vol. 208, no. 1, pp. 51–74, 2005.

[77] D. Murphy, D. Morra, and J. Katz, "Rain drops and oil slicks: Impact of water droplets on a surface oil layer," in *APS Meeting Abstracts*, 2013.

[78] J. Hnat and J. Buckmaster, "Spherical cap bubbles and skirt formation," *The Physics of Fluids*, vol. 19, no. 2, pp. 182–194, 1976.

[79] Z. Peng, Z. Yuan, T. Li, J. Cai, X. Wu, and F. Fan, "Research on multiphase flows in thermo-energy engineering institute of southeast university," *International Journal of Multiphase Flow*, vol. 36, no. 2, pp. 119–126, 2010.